Department of Materials Science and Engineering

Development of Multifunctional Magnetic Core Nanoparticles

Norsuria Mahmed

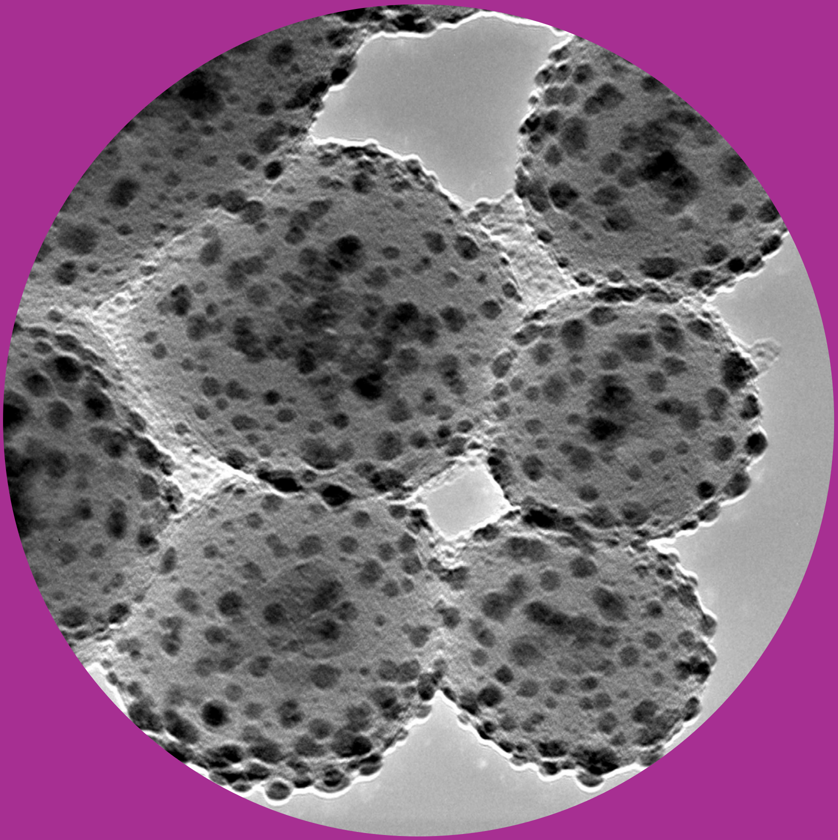

Aalto University

DOCTORAL
DISSERTATIONS

Aalto University publication series
DOCTORAL DISSERTATIONS 58/2013

Development of Multifunctional Magnetic Core Nanoparticles

Norsuria Mahmed

Doctoral dissertation for the degree of Doctor of Science in Technology to be presented with due permission of the School of Chemical Technology for public examination and debate in Auditorium V1 at the Aalto University School of Chemical Technology (Espoo, Finland) on the 26 April 2013 at 12 o'clock noon.

Aalto University
School of Chemical Technology
Department of Materials Science and Engineering
Advanced and Functional Materials Group

Supervising professor
Professor Simo-Pekka Hannula

Thesis advisor
Professor Simo-Pekka Hannula

Preliminary examiners
Professor Giorgio Piccaluga
Universita di Cagliari, Italy

Dr. Maria del Puerto Morales (Senior Scientist)
Instituto de Ciencia de Materiales de Madrid, Spain

Opponents
Professor Markku Leskelä
University of Helsinki, Finland

Aalto University publication series
DOCTORAL DISSERTATIONS 58/2013

ISBN 978-952-60-5105-5 (printed)
ISBN 978-952-60-5106-2 (pdf)
ISSN-L 1799-4934
ISSN 1799-4934 (printed)
ISSN 1799-4942 (pdf)
http://urn.fi/URN:ISBN:978-952-60-5106-2

Unigrafia Oy
Helsinki 2013

Finland

NORDIC ECOLABEL
441 697
Printed matter

Aalto University

Aalto University, P.O. Box 11000, FI-00076 Aalto www.aalto.fi

Abstract

Author
Norsuria Mahmed

Name of the doctoral dissertation
Development of multifunctional magnetic core nanoparticles

Publisher School of Chemical Technology

Unit Department of Materials Science and Engineering

Series Aalto University publication series DOCTORAL DISSERTATIONS 58/2013

Field of research Materials Science

Manuscript submitted 4 February 2013 **Date of the defence** 26 April 2013

Permission to publish granted (date) 19 March 2013 **Language** English

☐ **Monograph** ☒ **Article dissertation (summary + original articles)**

Abstract

Multifunctional magnetic materials have a great importance in various fields of application, e.g., material science, chemistry, physics, environmental chemistry and biomedicine. Although a large number of scientific papers already describe the synthesis of multifunctional materials by various methods and technologies, a simple, fast and economically feasible synthesis procedure to combine all the materials in one system is still of interest.

This thesis contributes to the development of multifunctional magnetic-core materials scientifically in three parts. Firstly, the synthesis of magnetic core, i.e., magnetite nanoparticles, was attempted using only ferrous ions (Fe^{2+}) of various concentrations as a magnetite precursor under ambient atmosphere. It was found that the synthesized magnetite was in a non-stoichiometric state, i.e., oxidation occurs. The introduction of Stöber silica (SiO_2) layer in the form of a coreshell structure prevented the oxidation of the synthesized particles, as suggested by the low temperature magnetic measurement and Mössbauer study. Secondly, this thesis introduces a simple, room temperature synthesis method for further functionalization of the magnetite-silica coreshell powders with silver (Ag) and silver/silver chloride (Ag/AgCl) nanoparticles. Based on the proposed approaches, the Ag deposition on the silica shells can take place by three possible mechanisms: a) absorption of Ag^+ on the silica surface by ionic bonding between the silver ions and hydroxyl groups (OH) of silica followed by the reduction of Ag^+ by polyvinylpyrrolidone (PVP), b) hydrogen bonding between the PVP-coated Ag and the SiO_2 shells, and c) electrostatic attraction between PVP-coated Ag and SiO_2 shells. The silver chloride particles are formed when a certain amount of hydrochloric acid (HCl) is introduced. The particle morphology is controlled by the concentration of HCl. Thirdly, the thesis makes a scientific contribution by introducing novel properties by compacting the magnetite-silica coreshell powders into bulk material by pulsed electric current sintering (PECS). By adjusting the amount of magnetite-core inside the silica structure, it is possible to produce a transparent magnetic compact. In addition, the effects of the sintering atmosphere and temperature on the final properties of the compacts were also studied.

Keywords magnetite, silica, silver, silver chloride, pulsed electric current sintering, phase transformation, multifunctional, ferromagnetic

ISBN (printed) 978-952-60-5105-5 **ISBN (pdf)** 978-952-60-5106-2

ISSN-L 1799-4934 **ISSN (printed)** 1799-4934 **ISSN (pdf)** 1799-4942

Location of publisher Espoo **Location of printing** Helsinki **Year** 2013

Pages 195 **urn** http://urn.fi/URN:ISBN:978-952-60-5106-2

Preface

First and foremost, I would like to raise my infinite thanks to God, the Most Gracious and the Most Merciful…Alhamdulillah.

The research work presented in this thesis was performed between the years of December 2008–December 2012 at Aalto University, which is formerly known as Helsinki University of Technology. The works were carried out at the School of Chemical Technology, Department of Materials Science and Engineering, under Advanced and Functional Materials (AFM) group.

The research and financial supports from Ministry of Higher Education Malaysia, Universiti Malaysia Perlis, The Finnish Academy via the Graduate School of Advanced Materials and Processes at Aalto University, and the Ella and Georg Ehrnrooth Foundation are gratefully acknowledged.

I have 'reported' to AFM group in November 2008 after the short 'phone interview' with the responsible person who brought me into the group. Thereby, I would like to express my most sincere gratitude and appreciation to my supervisor, Professor Simo-Pekka Hannula for accepting me as one of his doctoral students. His trust, supports, encouragement and faithful guidance were the main reason for the emergence of this thesis.

I would to thank the pre-examiners of my thesis, Professor Giorgio Piccaluga and Dr Maria del Puerto Morales for their reviews and comments in order to improve the quality of the thesis. My appreciation also goes to Professor Markku Leskelä, who became an opponent during the public examination of my thesis.

I would like to express my million thanks to Dr Oleg Heczko for his valuable help in my research work, especially in the magnetic measurement and Dr Outi Söderberg for her scientific guidance and advice. In addition, I wish to acknowledge all of the other co-authors of my Publications for their significant contributions to this thesis. Special thanks goes to Pirjo Korpiala for her guidance and practical help during my experimental work in the lab. Not to forget Dr Yanling Ge, my ‘lab roommate’, thank you for being a good listener during my ‘talkative’ time, giving the advice and motivation during my hard time, and thank you also for teaching me how to use the TEM. I will miss u.

For my friends and colleagues Juha, Vivek, Erkin, Riina, Raisa, Qian, Oskari, Sarianna, Jussi, Juho, Marjatta, Ilka A, Liu, Ilka P, Ulla, Eero and Risto; thank you very much for the friendship. I am glad to know all of you and you guys will always be in my heart. In addition, I really appreciate all the help given during my research work in the lab especially in conducting the lab equipments. For my Malaysian friends in Finland especially the Malaysian student’s families, thank you for all the enjoyable moments that we shared together throughout the years.

Finally, I would like to express my warmest gratitude to my parents, Mahmed Omar and Mek Yah Jusoh, my parents-in-law Abdullah Al-Hadi Muhamed and Aishah Hassan, and my siblings for their unconditional support, love and prayers. For my son Amir Hazeem Al-Hadi and daughter Anis Nur Iman, thank you for the love, understanding and nicely behaved during mama’s busy days. Mama loves you both a lot! People always said, ‘Behind Very Successful Man There is a Woman’. In my case, it is vice-versa; ‘Behind what I have achieved today, there is a good husband’. To Azremi Abdullah Al-Hadi, thank you for your love, prayers, patience, support, understanding and always by my side through my thick and thin.

Norsuria Mahmed
Espoo, March 2013.

List of Publications

This thesis consists of a summary of the author's work on the synthesis of magnetic nanoparticles, functionalizing the particles for possible multifunctional applications, consolidation of bulk materials thereof, and characterizing the powders and the bulk and their properties. The original research and results are presented in seven publications attached to this thesis and referred to in the text by the Roman numerals I-VII as follows:

Publication I

Mahmed, N., Heczko, O., Söderberg, O. & Hannula, S-P (2011) Room temperature synthesis of magnetite ($Fe_{3-\delta}O_4$) nanoparticles by a simple reverse co-precipitation method. *IOP Conference Series: Materials Science and Engineering*, 18, 032020.

Publication II

Mahmed, N., Heczko, O., Lancok, A. & Hannula, S-P. The magnetic and oxidation behavior of bare and silica-coated iron oxide nanoparticles synthesized by reverse co-precipitation of ferrous ion (Fe^{2+}) in ambient atmosphere. Submitted to *Journal of Magnetism and Magnetic Materials*.

Publication III

Mahmed, N., Jiang, H., Heczko, O., Söderberg, O. & Hannula, S-P (2012) Influence of different synthesis approach on doping behavior of silver nanoparticles onto the iron oxide-silica coreshell surfaces. *Journal of Nanoparticle Research*, 14, 987.

Publication IV

Mahmed, N., Heczko, O. & Hannula, S-P (2013) Influence of hydrochloric acid concentrations on the formation of AgCl-doped iron oxide-silica coreshell structures. *Advances in Science and Technology*, 77, 184–189.

Publication V

Mahmed, N., Heczko, O., Maki, R., Söderberg, O., Haimi, E. & Hannula, S-P (2012) Novel iron oxide-silica coreshell powders compacted by using pulsed electric current sintering: Optical and magnetic properties. *Journal of the European Ceramic Society*, 32, 2981–2988.

Publication VI

Mahmed, N., Friman, M. & Hannula, S-P (2012) Phase transformation of iron oxide-silica coreshell structure during differential scanning calorimetry and pulsed electric current sintering processes: A comparison. *Materials Letters*, 85, 18–20.

Publication VII

Mahmed, N., Larismaa, J., Heczko, O., Cura, M. E. & Hannula, S-P (2013) Influence of sintering temperature on the properties of pulsed electric current sintered hybrid coreshell powders. *Journal of the European Ceramic Society*. [Online].
Available from: http://dx.doi.org/10.1016/j.jeurceramsoc.2012.12.023
[Accessed 29th January 2013].

Brief Description of the Publications

Publication I: "Room temperature synthesis of magnetite ($Fe_{3-\delta}O_4$) nanoparticles by a simple reverse co-precipitation method"

This paper describes the synthesis of magnetite (Fe_3O_4) nanoparticles in air using only ferrous ions (Fe^{2+}) as a precursor and ammonium hydroxide (NH_4OH) as a precipitating agent. A room temperature reverse co-precipitation method was applied. Two synthesis protocols were used and the properties of the synthesized Fe_3O_4 nanoparticles were compared.

The effects of the synthesis protocols on the morphology, particle size, magnetic properties and oxidation behavior of the synthesized products were studied. Based on the results, it was suggested that the synthesis of magnetite in ambient atmosphere resulted in a non-stoichiometric state ($Fe_{3-\delta}O_4$) of the particles with the stoichiometry approaching magnetite depending on the Fe^{2+} concentrations and synthesis protocols used.

Publication II: "The magnetic and oxidation behavior of bare and silica-coated iron oxide nanoparticles synthesized by reverse co-precipitation of ferrous ion (Fe^{2+}) in ambient atmosphere"

In this work, the magnetic properties of the most oxidized magnetite nanoparticles synthesized from Publication I were studied at low temperature magnetic measurement. The oxidation behavior of the particles was studied by comparing Mössbauer spectroscopy results with X-ray diffraction (XRD) measurements. Freshly re-synthesized particles were then immediately coated with the silica (SiO_2) layer forming the coreshell structure by applying a modified Stöber method. The magnetic and oxidation behaviors of the coreshell structure were studied. Results suggest that the silica-shell can prevent further oxidation of magnetite and improve the magnetic properties of the nanoparticles.

Publication III: "Influence of different synthesis approach on doping behavior of silver nanoparticles onto the iron oxide-silica coreshell surfaces"

In this work, silver (Ag) nanoparticles were doped on magnetite-silica coreshell surfaces using four different synthesis approaches. The reduction of Ag ions (Ag^+) was done at room temperature in a solution containing polyvinylpyrrolidone (PVP) as a reducing agent. The attachment mechanism of the Ag nanoparticles was also studied.

Results suggest that Ag deposition on the silica shells can be based on three possible mechanisms: a) absorption of Ag^+ on the silica surface by ionic bonding between the silver ions and hydroxyl groups (OH) of silica followed by the reduction of Ag^+ by PVP, b) hydrogen bonding between the PVP-coated Ag and the SiO_2 shells, and c) electrostatic attraction between PVP-coated Ag and SiO_2 shells. It was found that the synthesis approach used had a major influence on the particle size distributions, magnetic behavior and optical properties of the final products.

Publication IV: "Influence of different hydrochloric acid concentrations on the formation of AgCl-doped iron oxide-silica coreshell structures"

Silver chloride (AgCl) particles were doped on the surface of magnetite-silica coreshell surfaces. The formation of AgCl particles is due to the reaction of Ag^+ and chloride ions (Cl^-) from hydrochloric acid (HCl). PVP as a capping agent controls the agglomeration and growth of AgCl particles. The size and shape of the AgCl particles formed was found to depend on the amount of HCl used. A very high concentration of Cl^- resulted in large particles with irregular cubic-like morphology, while at very low Cl^- concentration, small, nearly spherical AgCl nanoparticles were formed. In optical measurement, a broad absorption in the UV-visible wavelength suggested the co-existence of Ag nanoclusters.

Publication V: "Novel iron oxide-silica coreshell powders compacted by using pulsed electric current sintering: Optical and magnetic properties"

This paper describes the compaction of magnetite-silica coreshell powder synthesized using the Stöber method presented in Publication II. Pulsed electric current sintering (PECS) was used to produce bulk transparent magnetic compact by controlling the amount of magnetic particles inside the silica shells.

Results suggest that a high concentration of magnetite-core nanoparticles induced crystallization of the amorphous silica glass. Crystallization was due to the reduction of the magnetite into pure iron (Fe). The obtained microstructures were related to the transparency and the magnetization behavior of the compacts.

Publication VI: "Phase transformation of iron oxide-silica coreshell structure during differential scanning calorimetry and pulsed electric current sintering processes: A comparison"

The phase transformation of magnetite-silica coreshell structure was studied in two different heating environments. The coreshell powders were heated in a high-temperature differential scanning calorimeter in argon and sintered by PECS in a vacuum at a temperature of 1323 K.

Based on the results of this publication, it was suggested that in an argon atmosphere silica acted as a reducing agent by creating a mild hydrogen atmosphere from the hydrogen-bonded silica network. In PECS, the reducing environment came from the reaction of graphite foils in a vacuum during the sintering process. Both environments caused the reduction of the iron oxides.

Publication VII: "Influence of sintering temperature on the properties of pulsed electric current sintered hybrid coreshell powders"

In this work, three different types of hybrid coreshell powders, a) magnetite-silica, b) magnetite-silica-silver and c) silica-silver, were compacted using the PECS method. The pressure and time for sintering was kept constant, while the temperature was varied from 873–1273 K in order to determine its influence on compaction.

Based on the results, it was suggested that at PECS compaction temperature higher than 1173 K resulted in the reduction of iron oxide into pure iron (Fe) and crystallization of an amorphous SiO_2. In Ag-containing compacts, silver oxides were found to be intermediate phases during the formation of metallic Ag. Thermal decomposition of these oxides resulted in the oxidation of magnetite into hematite (α-Fe_2O_3), which caused a large drop in saturation magnetization values. Increasing the sintering temperature had a small impact on improving the density and a decisive effect on the magnetite state of the composites. The estimated relative densities within 58–68% for all the compacts showed that porous structures were obtained.

Author's Contribution

The author of this thesis is the responsible author for the publications (I-VII) presented in this thesis. The author has also performed the majority of the research presented in the publications. The author has been involved in writing the research plans, designing the experiments and planning the manuscripts for publication. The author is fully responsible for the experimental part related to the synthesis of the magnetic nanoparticles, functionalization of the nanoparticles with the silica coating, and doping of silver and silver chloride onto the silica surfaces. In characterization, the author is responsible for the XRD, SEM, TEM, UV-Vis and Archimedes Density studies of the synthesized products. The author is mainly responsible for writing the draft manuscripts.

The contributions of the co-authors to the experimental work and preparation of the manuscripts are listed below:

- Professor Simo-Pekka Hannula provided the original idea for the research and important scientific guidance in preparing and conducting the research work. He has also guided in preparing and reviewing the manuscripts prior to their submission for publication.

- Dr. Oleg Heczko provided his expertise in magnetic measurement and analysis and helped the author in writing the magnetic results in Publications I, II, III, IV, V and VII. He also contributed in the Mössbauer study for Publication II.

- Dr. Outi Söderberg guided the research work and in reviewing the manuscript for Publications I, III and V.

- Dr. Hua Jiang provided his expertise in high-resolution TEM studies for Publication III.

- Dr. Adriana Lancok provided her expertise in Mössbauer spectroscopy measurement and analysis and in writing up the Mössbauer results in Publication II.

- MSc. Juha Larismaa provided his expertise in annealing and sintering of silver-doped silica structures and contributed in the density measurement for Publication VII.

- MSc. Ryuji Maki contributed in powder compaction using PECS for Publication V.

- MSc. M. Erkin Cura contributed in powder compaction using PECS for Publication VII.

- MSc. Michael Friman contributed in high temperature differential scanning calorimetry (DSC) measurements for Publication VI.

- MSc. Eero Haimi provided guidance on the optical spectroscopy study in Publication III.

Professor Simo-Pekka Hannula

Espoo, February 4th, 2013

Contents

- 2.2. Particle synthesis

2.4. Characterization of materials

List of Abbreviations

3Y-TZP	3 mol% yttria-doped tetragonal zirconia polycrystalline
ccp	cubic closed-packed
DMSO	dimethyl sulfoxide
DNA	deoxyribonucleic acid
DSC	differential scanning calorimetry
DTC	dithiocarbamate
ECAS	electric current assisted sintering
EDS	energy dispersive spectroscopy
FAST	field assisted sintering technique
FM	ferri-/ferromagnetic
FWHM	full-width-half-maximum
HAADF	high-angle annular dark-field
hcp	hexagonal closed-packed
HIP	hot isostatic pressing
HP	hot pressing
NBO	non-bridging oxygen
NIR	near-infrared
PECS	pulsed electric current sintering
PPMS	physical property peasurement system
PVP	polyvinylpyrrolidone
SAED	selected-area-electron-diffraction
SDS	sodium dodecyl sulfate
SEM	scanning electron microscope
SERS	surface-enhanced raman scattering
SP1	synthesis protocol 1
SP2	synthesis protocol 2
SPM	superparamagnetic

SPS	spark plasma sintering
ssDNA	single-stranded deoxyribonucleic acid
STEM	scanning transmission electron microscope
TEM	transmission electron microscope
TEOS	tetraethylorthosilicate
TGA	thermogravimetric analysis
UV-Vis	UV-visible spectrometer
VSM	vibrating sample magnetometer
XRD	X-ray diffraction

Nomenclature

$=Si(OH)_2$	silanediols
≡Si-OH	silanol
≡Si-O-Si≡	siloxane
a	unit cell length
AgCl	silver chloride
$AgNO_3$	silver nitrate
B	full-width-half-maximum
CoO	cobalt oxide
CuO	copper oxide
EtOH	ethanol
Fe or α-Fe	pure iron
$Fe(C_5H_5)_2$	ferrocene
$Fe(OH)_2$	iron (II) hydroxide
$Fe(OH)_3$	iron (III) hydroxide
$Fe_{2.67}O_4$	maghemite stoichiometry
Fe^{2+}	ferrous ion
Fe^{3+}	ferric ion
Fe_3O_4	magnetite
$Fe_{3-\delta}O_4$	non-stoichiometric magnetite
FeO	wustite
FeOOH	iron oxide-hydroxide
$FeSO_4\cdot 7H_2O$	ferrous sulfate
H_C	coercivity
HCl	hydrochloric acid
M	molar
$MgAl_2O_4$	magnesium aluminate
M_R	remanence

M_S	saturation magnetization
M_T	molar mass
$NaBH_4$	sodium borohydrate
NaOH	sodium hydroxide
NH_4OH	ammonium hydroxide
OH	hydroxyl
SiC	silicon carbide
SiO_2	silica
t	estimate of the crystallite size
T_B	blocking temperature
T_C	Curie temperature
TiO_2	titanium dioxide
T_N	Neel temperature
T_V	Verwey transition temperature
V_m	molar volume
W_P	weight fraction of the powder
x	Fe^{2+}/Fe^{3+}
ZnO	zinc oxide
α-Al_2O_3	corundum
α-Fe_2O_3	hematite
γ-Fe_2O_3	maghemite
δ	stoichiometry deviation
ε-Fe_2O_3	ε-iron oxide
θ_B	Bragg angle
λ	X-ray wavelength of the source material
ρ	density
ρ_P	theoretical density of the powder
ρ_T	theoretical density of the mixture

List of Figures

List of Tables

1. Introduction

The concept of ‘multifunctional material’ can be defined as any material or material-based system that integrally combines two or more properties, i.e., a structural property with an additional functionality such as optical, magnetic, thermal, or electrical in order to satisfy previously unattainable performance metrics. Multifunctional materials can also simply be defined as designed to meet specific requirements through tailored properties. Multifunctional materials can cover a broad area of science, including materials science, chemistry, physics, and biotechnology.

In this thesis the development of magnetic materials, especially iron oxide nanoparticles, as multifunctional materials is studied and reviewed. Iron oxide nanoparticles, in particular magnetite (Fe_3O_4) particles, are amongst the most popular materials that have been applied to environmental chemistry, analytical biochemistry, medicine and biotechnology. However, many difficulties arise when pure magnetic nanoparticles are directly exposed to the application system, including effects on ease of aggregation, stabilization and biodegradation. Therefore, many of these particles are usually used in the form of a magnetic core, which is coated by various organic and inorganic species for multifunctional applications. For example, magnetic nanoparticles for in vivo biomedical use must be small enough to avoid detection by the immune system and to be circulated through the blood stream, and they should be stable enough to remain in the body for a sufficient time. Coating them with a biologically compatible substance will make them suitable for those specific applications. In addition, multifunctional magnetic particles maybe designed to be re-used or recycled due to their tailored magnetic properties.

The coating materials for surface modification of the magnetic nanoparticles must have good chemical stability. In addition to maintain the stability and protecting the particles from degradation at high temperature, and oxidation by oxygen or erosion by acids or bases, the coating materials must also be compatible with various organic and inorganic species. By these abilities, a multifunctional coreshell structure can be further developed by doping the structure with metal species or functional groups. Even though a large number of scientific papers already describe the synthesis of multifunctional materials by various methods and technologies, a simple, fast and economically feasible synthesis procedure to combine all the materials in one system is still of interest. Consequently, novel synthesis methods need to be developed.

In the context of multifunctional coreshell structures, most of the research focuses on their properties and applications as powders. Only a few studies focus on transferring these properties into a bulk structure and studying their properties. In this thesis, emphasis is not only on synthesizing of multifunctional material based on the coreshell particles but also on investigating novel and interesting properties of the materials when they are transferred into bulk materials. It is hoped that the results of this research can be used in the further development of multifunctional nanopowders.

1.1 Iron oxide nanoparticles

Iron oxides are compounds that are widespread in nature, and they have also been synthesized in the laboratory. They exist in many forms, including oxides, hydroxides and oxide-hydroxides. Among them, magnetite (Fe_3O_4), maghemite (γ-Fe_2O_3) and hematite (α-Fe_2O_3) are the most commonly used in various technological applications (Kumar, 2009). Hematite, which is also known as ferric oxide, iron sesquioxide, red ochre, martite and kidney ore among others, is the oldest known iron oxide and is widespread in rock and soils (Cornell & Schwertmann, 2003). The color of hematite in fine powder form is blood-red, while in the coarsely crystalline form the color is black or grey (Cornell & Schwertmann, 2003; Schwertmann, 2008).

Hematite is extremely stable in ambient conditions and is usually the end product in transformations of other iron oxides. The hematite has the corundum (α-Al_2O_3) structure that is based on hexagonal closed-packed (hcp) anion packing, with Fe (III) ions occupying the octahedral sites (Schwertmann et al., 1979; De Grave et al., 1988). Magnetite (Fe_3O_4), also called black iron oxide, tri-iron tetraoxide and ferrous ferrite, is a common end product of biological and abiotic reduction of ferric (Fe^{3+}) oxides in natural environments (Cornell & Schwertmann, 2003). It exhibits the strongest magnetism of any transition metal oxide (Maher, 1988; Kletetschka, Wasilewski & Taylor, 2000). Maghemite is a red-brown iron oxide that occurs in soils as a weathering product of magnetite or as a product of heating of other iron oxides (Cornell & Schwertmann, 2003). Maghemite crystallizes in a spinel structure with 32 O^{2-} ions; eight Fe^{3+} ions located in tetrahedral sites (A-sites) and sixteen Fe^{3+} ions in octahedral sites (B-sites), per unit cell. It has the same crystal structure as magnetite and can be considered as an Fe (II)-deficient magnetite (Cornell & Schwertmann, 2003; Teja & Koh, 2009; Gorski & Scherer, 2010).

1.1.1 Magnetite nanoparticles

Magnetite has become an important mineral/iron ore in several fields of study. For example, magnetite has widespread applications such as ferrofluids, targeted drug delivery, digital media recording, magnetic resonance imaging, magnetic hyperthermia, etc. (Raj & Moskowitz, 1990; Pankhurst et al., 2003; Guo et al., 2009). Magnetite is also a facile reductant for several environmental contaminants found in groundwater (McCormick, Bouwer & Adriaens, 2002). It is also used in waste-water treatment as an effective sorbent for many contaminants that can easily be separated from water by an applied magnetic field (Girginova et al., 2010).

Magnetite has an inverse spinel structure with an Fd3m space group (Bragg, 1915). The unit cell length is $a = 0.839$ nm, with eight formula units per unit cell. Magnetite has an oxygen cubic close-packed (ccp) structure that contains both divalent and trivalent iron with trivalent ions occupying both tetrahedral and octahedral sites. Thus the magnetite formula can be precisely written as (Akimoto, 1954; Gorski & Scherer, 2010):

$$^{Tet}Fe^{3+}\left[^{Oct}Fe^{2+}Fe^{3+}\right]O_4 \qquad (1.1)$$

The ^{Tet}Fe is often referred to as the "A" site, and the ^{Oct}Fe is denoted as the "B" site. There are eight $^{Tet}Fe^{3+}$, eight $^{Oct}Fe^{2+}$, eight $^{Oct}Fe^{3+}$ and 32 O atoms within the unit cell. Magnetite is frequently non-stoichiometric; it can have a range of oxidation states dependent upon the amount of structural Fe^{2+}. In stoichiometric magnetite, $x = Fe^{2+}/Fe^{3+} = 0.5$. When magnetite is oxidized, the Fe^{2+}/Fe^{3+} ratio decreases ($x < 0.50$), and this form is expressed as non-stoichiometric or partially oxidized magnetite. In non-stoichiometric magnetite, the structure is written as $Fe_{3-\delta}O_4$. δ can range from 0 for stoichiometric magnetite to 0.33 for completely oxidized magnetite, which is also called maghemite (γ-Fe_2O_3). This formula can be expressed as (Hägg, 1935; Gorski & Scherer, 2010):

$$^{Tet}Fe^{3+}\left[^{Oct}Fe^{2+}_{1-3\delta}Fe^{3+}_{1+2\delta}[\,]\right]O_4 \qquad (1.2)$$

where [] refers to the vacancies formed in the crystal structure to counter the charge balance. The relationship between the stoichiometry and δ can be written as (Gorski & Scherer, 2010):

$$x = \frac{Fe^{2+}}{Fe^{3+}} = \frac{1-3\delta}{2+2\delta} \qquad (1.3)$$

Many researchers have already studied the preparation of magnetite nanoparticles with different characteristics and purposes. Methods used include thermal decomposition (Guardia et al., 2007; Maity et al., 2009), hydrothermal treatment (Chen et al., 2009), co-precipitation (Liu et al., 2004; Marinescu et al., 2006; Murbe, Rechtenbach & Tőpfer, 2008), sol-gel (Xu et al., 2007), electro-precipitation (Marques et al., 2008), forced hydrolysis (Compeán-Jasso et al., 2008), solvothermal (Guo et al., 2009) and microemulsion (Gupta & Wells, 2004) techniques. Of all the methods mentioned above, co-precipitation is the most common method used to produce magnetite nanoparticles due to its ease of use, large volume capability and economy. The co-precipitation process involves the precipitation of iron precursors Fe^{2+} and Fe^{3+} in the ratio of 1:2 by using an alkali, usually sodium hydroxide (NaOH) or ammonium hydroxide (NH_4OH), which leads to the formation of green rust at the early stage of precipitation, followed by the black solution after the precipitation process is completed. Many approaches have been taken for chemical co-precipitation of magnetite nanoparticles. These include co-precipitation in water/aqueous solutions using various types of alkalis and organic and amino acid solutions (Liu et al., 2004; Marinescu et al., 2006; Murbe, Rechtenbach & Tőpfer, 2008). Since the pH of the alkaline solution plays an important role in controlling the growth and size of the synthesized nanoparticles (Tang et al., 2009), the reverse co-precipitation method was applied by Aono et al. (2005) in synthesizing fine magnetite powder. Their work was inspired by the method reported by Teraoka et al. (1995), where the reverse co-precipitation method was used in synthesizing fine powders of poly-metallic oxides. In this technique, the iron precursor solution is dropped directly into the alkaline solution, in contrast to normal co-precipitation where the alkaline solution is added into the iron precursor solution. Thus the pH of the solution can be maintained during the precipitation process.

Alibeigi and Vaezi (2008) reported on reverse co-precipitation of ferrous/ferric (Fe^{2+}/Fe^{3+}) mixed salt in sodium hydroxide solution in an oxidizing environment, which resulted in the formation of maghemite, γ-Fe_2O_3, instead of magnetite particles due to the oxidation of Fe^{2+} to Fe^{3+}. They also found that reverse co-precipitation from a solution of only ferrous ions (Fe^{2+}) in air can be used to produce Fe_3O_4 phase nanoparticles. Mizukoshi et al. (2009) reported on ultrasonic-assisted reverse co-precipitation of ferrous sulfate ($FeSO_4 \cdot 7H_2O$) in an NaOH solution in various types of atmospheres, including air, with the addition of surfactant, which results in formation of Fe_3O_4 structures. Since, according to the literature, it is possible to produce magnetite nanoparticles in ambient atmosphere by using a reverse co-precipitation of ferrous ions, this method was applied in this thesis with some modifications. In addition, the application of vacuum or inert atmosphere during the synthesis can be eliminated, which is cost-saving. Furthermore, it is interesting to know how the Fe^{2+} precursor of various concentrations will affect the composition and magnetic behavior of the final products.

1.2 Magnetic properties of iron oxide nanoparticles

In general, magnetic materials can be classified as paramagnetic, ferrimagnetic, ferromagnetic or antiferromagnetic (Fig. 1.1). The magnetic behavior is strongly size dependent, and at a particular temperature, behavior may be altered by tuning the size of the constituent. In *paramagnetic* material, the magnetic dipoles are randomly oriented and can be aligned along their direction with the presence of the magnetic field. With the absence of a magnetic field, neither coercivity (H_C) nor remanence (M_R) can be observed (Fig. 1.2), meaning that the magnetic dipoles will randomize again without extra energy needed to demagnetize the material. A nanoparticle that exhibits this behavior is called *superparamagnetic* (SPM). Superparamagnetism is the size effect of ferromagnetism (Pankhurst et al., 2003). Superparamagnetic material has a single domain structure, which can fluctuate randomly by thermal fluctuation at high enough temperatures similar as an atom spin in paramagnetic materials (Cullity and Graham, 2009). At low temperature, the thermal energy becomes smaller and the magnetic moments become blocked. This temperature is the blocking temperature (T_B). Below blocking temperature, superparamagnetic material looses its preferred direction of magnetization in zero magnetic fields (Goya and Morales, 2004). For a *ferromagnetic* material, the magnetic dipoles align one to the other, which exhibits and enhances the collective response even in the absence of a magnetic field. In ferromagnetic material, there are three parameters that can describe the strength and the magnetization of the material: coercive field (H_C), saturation magnetization (M_S) and remanence (M_R). H_C is the external field required to reduce the magnetization back to zero, which also is related to the minimum energy needed for the reversal of the magnetization of the material. M_S shows the maximum value of the magnetization that the material can reach under a sufficient magnetic field, while M_R indicates the residual magnetization at zero applied field. These three parameters can be identified in the hysteresis loop generated in field-dependent magnetization measurements, as shown in Fig. 1.2 (Figuerola et al., 2010). In contrast to the ferromagnetic behavior, the neighboring magnetic dipoles can align in antiparallel (cancelling each other), which leads to two different situations: *antiferromagnetism* and *ferrimagnetism*. *Antiferromagnetism* occurs, when the antiparallel magnetic dipoles are of the same magnitude and possess no magnetic moment. *Ferrimagnetism* occurs when two coupled magnetic dipoles show different values, and in this case a net magnetic pole other than zero will still magnetize the material, even in the absence of an external magnetic field.

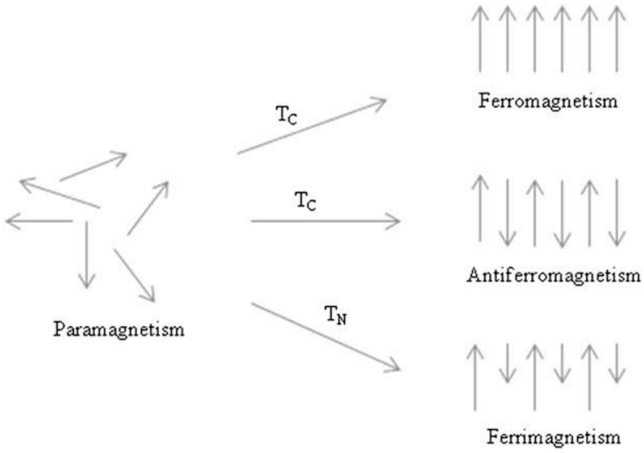

Fig. 1.1 Different orientations of magnetic dipoles. Reprinted from Teja & Koh (2009) with permission from Elsevier.

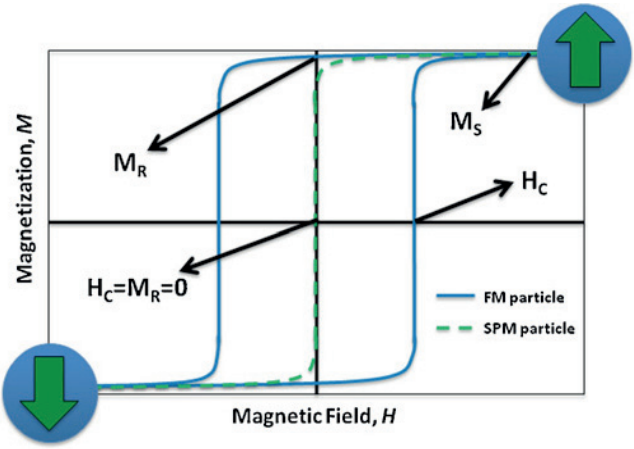

Fig 1.2 Theoretical magnetic field curve for superparamagnetic (SPM) and ferri- or ferromagnetic (FM) nanoparticles, where the coercive field (H_C), saturation magnetization (M_S) and remanent magnetization (M_R) parameter are indicated. Reprinted from Figuerola et al. (2010) with permission from Elsevier.

The ordered arrangement of magnetic moments decreases with increasing temperature due to thermal fluctuations of the individual moments. Beyond a certain transition temperature, the material becomes disordered and loses its magnetization. The transition temperature is termed the Curie temperature, T_C, for ferromagnetic and ferrimagnetic substances and the Neel temperature, T_N, for antiferromagnetic substances. Ferromagnetic or ferrimagnetic material undergoes a transition to a paramagnetic state above its T_C (Cullity and Graham, 2009). Hematite is paramagnetic above the Curie temperature (956 K), while at room temperature it is weakly ferromagnetic and undergoes a phase transition at 260 K (the Morin temperature, $T_{M)}$ to an antiferromagnetic state (Morin, 1950; Cornell & Schwertmann, 2003). The magnetic behavior of hematite mostly depends on the crystallinity, particle size and cation substitution (Bodker & Morup, 2000; Raming et al., 2002; Cornell & Schwertmann, 2003; Teja & Koh, 2009). Magnetite is ferrimagnetic at room temperature and has a Curie temperature of 850 K (Cornell & Schwertmann, 2003). Nevertheless, the term ferromagnetic is generally used for magnetite nanoparticles because in the magnetite inverse spinel structure, the anti-parallel Fe^{3+} spins on the octahedral and tetrahedral sites cancel out their magnetic contributions, and the ferromagnetic effect is provided by the Fe^{2+} ions in the octahedral sites. If the Fe^{2+} ions in some of the octahedral sites were oxidized, the M_S would decrease. Room temperature superparamagnetism in magnetite nanoparticles can be observed when the particle size is smaller than 6 nm, even though their magnetic behavior is strongly dependent on the synthesis method (Margulies et al., 1996; Sena et al., 1997; Voogt et al., 1998; Teja & Koh, 2009). It has been reported that the magnetic properties of nano-sized magnetite depend strongly on the crystal morphology, where the morphology affects the coercivity, which increases in the order of spheres < cubes < octahedral. Magnetite nanoparticles with coercivity values ranging from 2.4 to 20 kA/m have been produced by controlling their synthesis conditions (Meisen & Kathrein, 2000; Cornell & Schwertmann, 2003). Maghemite, the fully oxidized magnetite, is ferrimagnetic at room temperature, unstable at high temperatures, and loses its susceptibility with time (Dronskowski, 2001). The T_C of maghemite is difficult to determine because maghemite transforms to hematite above 400 K, with a consequent dramatic loss of magnetization. Nevertheless, the Curie temperature is believed to be between 820 K and 986 K (Cornell & Schwertmann, 2003).

Surface effects are found to have a strong influence on the magnetic properties of iron oxide nanoparticles (Tronc et al., 2000). As a consequence, their net magnetization decreases at a faster rate with increasing temperature than that of the corresponding bulk material because a large fraction of the atoms are near the surface, where the exchange field is lower (Hendriksen, Linderoth & Lindgárd, 1993; Morales et al., 1997). Surface modifications of iron oxide nanoparticles by chemical treatments have become an option in controlling the magnetic behavior, such as coercivity, of the iron oxide nanoparticles (Itoh & Satou, 1975; Spada, Berkowitz & Prokey, 1991). In addition, novel multifunctional properties might also be aroused.

1.3 Coreshell structures

The expression ‘coreshell’ is used for a structure that consists of a material or particle-core that is coated by an outside layer forming a shell around the core. The purpose of this structure is based on two main ideas. The first idea is to protect the individual particles against the degradation agents while retaining their intrinsic properties (Varanda, Jafelicci & Goya, 2001). The second idea is to improve or create novel properties that cannot be obtained by a single particle. Iron oxide nanoparticles, especially nano-sized magnetite, are highly susceptible to oxidation when exposed to air due to the large surface area. These particles also easily form agglomerates due to inter-particle attraction and thus may lose the properties associated with their nanostructures, such as lower magnetization values. In addition, for certain applications, e.g., biomedical applications, protection of the magnetic particles from erosion by acids or bases also needs to be considered. Based on these issues, all the protection strategies result in magnetic nanoparticles with a coreshell structure. Various coating materials have been introduced as the shell structure, including metal oxides, polymers, precious metals, and silica (Lu, Salabas & Schuth, 2007).

Surface passivation by mild oxidation is one of the approaches used to protect the magnetic-core nanoparticles. In this approach, a metal oxide layer is introduced on the outer surface of the core particles. For example, Boennemann et al., (2003) used synthetic air to oxidize as-synthesized cobalt nanoparticles to form a stable cobalt oxide (CoO) outer layer that can prevent oxidation of the cobalt core.

Surfactants or stabilizers such as oleic acid, polyvinyl alcohol, dextran and sodium dodecyl sulfate (SDS) (Berry et al., 2003; Farrell, Majetich & Wilcoxon, 2003; Cannas et al., 2010) have been used to coat the magnetic particles in order to prevent aggregation due to van der Waals forces and inter-particle interactions between the particles. Thus these polymers can be anchored or adsorbed on the magnetic particles to form layers that create steric repulsion to balance those forces and stabilize the nanoparticles in the solution. However, for certain applications the magnetic coated polymer layers are not stable and are easily leached by acidic solution (Farrell, Majetich & Wilcoxon, 2003), which causes a loss in their magnetic properties. In addition, a thin polymer coating is insufficient to prevent oxidation of the highly reactive metal particles and is unsuitable for high temperature applications due to its low intrinsic stability; therefore, alternative coating materials should usually be considered.

Magnetic nanoparticles have also been directly coated with precious/noble metals such as gold and silver or metal oxides such as titania (TiO_2) or zinc oxide (ZnO) (Watson, Beydoun & Amal, 2002; Iglesias-Silva et al., 2007; Wan, Li & Chen, 2009; Kalska-Szotsko et al., 2012). For example, in order to impress the optical properties of the magnetic core, silver-coated magnetite nanoparticles have been produced (Iglesias-Silva et al., 2007). A two-step procedure was used: in the first step, the magnetite-core was synthesized using a microemulsion method, and in the second step, silver ions were absorbed on magnetite-core surfaces, followed by reduction by glucose, forming the silver metal layer. In addition to silver, gold has also been an ideal coating metal due to its low reactivity, and its surface can be further functionalized with thiol groups. Kalska-Szostko et al. (2012) synthesized the magnetite-gold coreshell structure, which was further functionalized with hexamedicanethiol for immobilization of biological molecules such as trypsin and glucose oxidase. However, direct coating with gold can also be very difficult due to the dissimilar nature of the two surfaces (magnetite and gold). In the case of a magnetite-titania coreshell structure (Watson, Beydoun & Amal, 2002), a sol-gel method was applied to form the amorphous titania shell, followed by a heat treatment process to transform this amorphous phase into a photoactive titania shell. The advantage of this coreshell structure is that a recyclable photocatalyst with a magnetic core can be produced. However, direct coating of these metal nanoparticles can cause a direct electrical contact that results in a high level of photodissolution (Beydoun et al., 2002). The heat treatment also affects the photoactivity, stability and strength of the magnetic properties of the coated particles. For example, excessive heat treatment of iron oxide/titania systems destroys the hydroxyl groups on the titania surface, which affects the photoactivity. At the same time, the heat treatment may also result in partial oxidation of the magnetic iron oxide core and hence decrease the magnetic properties of the prepared photocatalyst (Beydoun et al., 2000). Thus a more inert and chemically stable coating material (silica) was introduced by Beydoun et al. (2002) to act as a barrier between the two metals/metal oxide.

1.3.1 Silica coating

Coating magnetic nanoparticles with an amorphous silica layer is a promising and important approach in the development of magnetic nanoparticles for both fundamental study and technological applications. This is due to the properties of the silica itself. It is chemically inert and has high stability against aggregation, and silica formed on the surface of magnetic nanoparticles can screen the magnetic dipolar attraction between the core particles that favors the dispersion of magnetic nanoparticles in liquid media. Furthermore, surface modifications are easy due to the existence of abundant silanol groups on the silica layer that are compatible with various organic and inorganic species. A silica-coated magnetic nanoparticle has strong magnetic susceptibility and minimal residual magnetism, and interparticle interactions are easily controlled.

Many methods have been used for the synthesis of magnetic-silica coreshell structures. The most frequently reported routes include microemulsion, aerosol, silicic acid and the Stöber sol-gel process (Melancon & Li, 2009). In the microemulsion method, non-ionic surfactants such as Brij30 (Santra et al., 2001) Igepal CO-520 (Zhang, Cushing & O’Connor, 2008), Tritron-X (Yan, Yin & Zhou, 2006) are used in the formation of micelles and inverse micelles. These micelles are used to confine and control the silica coating that is formed around the magnetic nanoparticles by hydrolysis and condensation of tetraethyl orthosilicate (TEOS). The aerosol pyrolysis method involves the reaction of silica precursor and iron complex in the gaseous phase. For example, Bomati-Miguel et al. (2005) used ferrocene, $Fe(C_5H_5)_2$ and TEOS in toluene as precursors. These mixtures are then nebulized by an ultrasound method and the cloud formed is carried by a gas flux to the reactor to intersect a horizontal CO_2 laser beam, which initiates and sustains the reaction. Another method is silica coating via silicic acid formation (Liu et al., 2004). In this process, hydrochloric acid is added to the silica precursor, sodium silicate (Na_2SiO_3), and silicic acid is formed. The hydrolysis and condensation of this acid transforms the silanol groups (Si-OH) formed into siloxane bonds (Si-O-Si). A further polymerization process creates silica layers around the magnetic nanoparticles.

The Stöber method is the most elegant, simple and fast sol-gel method for preparing monodisperse spherical silica particles with diameters between 20 nm and 2000 nm. The process involves hydrolysis and condensation of a silica precursor such as TEOS in an ethanolic medium in the presence of ammonia at room temperature (Stöber, Fink & Bohn, 1968). The thickness of the silica coating can be adjusted by varying the amount of TEOS. The magnetic nanoparticles, especially iron oxides, have a positive surface charge, thus creating a strong affinity towards the negatively charged silica shell. Therefore, prior surface treatments of the iron oxide particles are not necessary. A few modifications of the Stöber method for the synthesis of magnetic-silica coreshell structures have been made. For example, Deng et al. (2005) coated the magnetite nanoparticles in a basic alcohol/water mixture using magnetic fluids as seeds. The magnetic fluid was first diluted with water and ammonium hydroxide and dispersed homogenously. TEOS was slowly added into the dispersion under continuous mechanical stirring. Silica was formed on the surface of magnetite nanoparticles through the hydrolysis and condensation of TEOS. Lu et al. (2008) developed a facile method for the synthesis of silica-coated magnetite nanoparticles by direct introduction of the magnetite core into the Stöber process upon the formation of the primary silica particles. The process is illustrated in Fig. 1.3. When TEOS, ammonia, water and ethanol are mixed together, the hydrolysis of TEOS results in the formation of silicic acid. The acid then condenses into small primary silica particles less than 5 nm in size. These primary silica particles are colloidally unstable and ready to aggregate into larger particles. The addition of magnetite nanoparticles during the aggregation of the primary silica results in the nanoparticles aggregating with each other or with primary silica due to the chemical affinity of their surface to silica. With an appropriate amount of primary silica, the magnetite nanoparticles can be surrounded by the primary silica particles, and further deposition of silica allows the formation of Fe_3O_4/SiO_2 composite nanoparticles. Even though the formation of silica coating by applying the Stöber method seems to be easy, the reaction parameters, including the type of alcohol, the volume ratio of alcohol to water, the amount of catalyst and the amount of precursor, play important roles in the successful application of the process.

Since the Stöber process promotes the low-cost, mild reaction, easy handling and surfactant-free synthesis of silica particles, this method has become dominant in the preparation of silica-coated magnetic particles as well as other particles such as noble metal species and metal oxides. Based on these advantages, the Stöber method was used to form the magnetite-silica coreshell structure in this thesis.

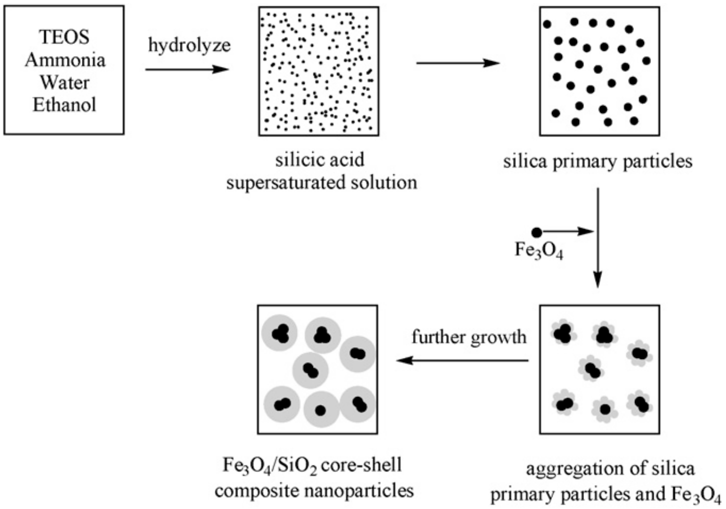

Fig. 1.3 Schematic illustration of the mechanism of silica particle nucleation by aggregation of primary silica particles and formation of magnetite-silica coreshell structures. Reprinted from Lu et al. (2008) with permission from Elsevier.

1.4 Multifunctional magnetic-silica coreshell structures

A silica shell not only acts as a protective layer for the magnetic core, but it can also act as an intermediate layer that inhibits direct contact of the core with additional functional groups or metal/metal oxides species from the unwanted interactions, for example, to prevent the direct contact of a titania shell with a magnetic core that can affect the efficiency of the photocatalyst (Beydoun et al., 2002) or to prevent the direct attachment of dye molecules such as Rhodamine B to magnetic nanoparticles that can result in luminescence quenching (Caruana et al., 2012). On the amorphous silica surfaces, the structures terminate either in siloxane groups (≡Si-O-Si≡) with oxygen atoms on the surface or in hydroxyl (OH) groups. There are three types of OH groups: a) isolated/single silanols (≡Si-OH), b) geminal/silanediols [$=\mathrm{Si}-(\mathrm{OH})_2$] and c) vicinal or H-bonded silanols, H-bonded silanediols and their H-bonded combinations (Zhuravlev, 2000). These groups are compatible with various organic and inorganic species, such as polymer functional groups and metal/metal oxide species. Thus, in addition to acting as inhibitor layers, the existence of these hydroxyl groups on the silica surface can expand the multifunctionality of the coreshell structures.

Many works have been reported on the application of functional groups such as amines, thiols and carboxyl groups in combination with magnetic-silica coreshell structures (Ashtari et al., 2005; Girginova et al., 2010; Hakami, Zhang & Banks, 2012). With these functional groups, biological molecules such as proteins, drugs, antibodies, enzymes, etc., can be covalently bonded on a functionalized silica surface and used for biomedical applications or wastewater treatments. For example, Girginova et al. (2010) functionalized magnetite-silica coreshell particles with dithiocarbamate (DTC) for removal of mercury ions, Hg^{2+}, from water. In a biomedical application, Ashtari et al. (2005) improved the method of recovery of the target single-stranded deoxyribonucleic acid (ssDNA) based on amino-modified silica-coated magnetic nanoparticles. The amino functional group was used in the immobilization of the DNA probe (ssDNA capture) on the coreshell particles through streptavidin conjugation using covalent bonds.

During the reaction, the ssDNA target hybridized with the DNA probe to form DNA bio-conjugate and separated from the solution under a magnetic field. With a combination of these materials, an effective, selective and very fast method for the recovery of target ssDNA and other viruses has been introduced, which is important for disease and mutation detection.

In addition to functional groups, metallic nanoparticles such as gold can be used for multifunctional magnetic-silica coreshell structures. Direct coating of gold onto iron oxide nanoparticles can produce a magnetic coreshell structure with plasmon resonance of about 500–600 nm. By introducing a dielectric silica layer in between the gold and iron oxide, this plasmon resonance can be tuned over 600–1500 nm, which can absorb the light in the near-infrared (NIR) region. In the NIR region, tissue transmissivity is highest due to low scattering and absorption (Ashtari et al., 2005). In addition, the gold surface is also compatible with thiol functional groups such as thiolated dextran (Choi et al., 2010) to mediate photothermal ablation of cancer cells. On this basis, it can be concluded that the multifunctionality of magnetic-core nanoparticles is not only obtained by functionalization with functional groups or metal species separately but also by the combination of both species. Besides gold, other metals such as silver nanoparticles are also important in multifunctional magnetic-silica coreshell applications.

1.4.1 Functionalization with silver nanoparticles

Noble metal such as silver (Ag) nanoparticles, especially colloidal silver particles, are very popular for applications in optics, catalysis, antimicrobiology, microbiology and optoelectronics (Evanoff & Chumanov 2005; Wiley et al., 2006; Xu et al., 2006; Raheman et al., 2011). However, in certain cases, such as a catalytic process in a solution, the bare Ag particles can be very active and easily form an aggregate due to the Van der Waals forces and high surface energy. This aggregation deactivates and poisons the catalysts during the catalytic reaction (Jiang, Liu & Sun, 2005). Thus Ag particles can be coated with an amorphous silica layer (Kobayashi et al., 2005) or immobilized on the substrate, which can effectively prevent the Ag nanoparticles from agglomeration in the form of core-shell nanostructures. Many researchers have reported using amorphous silica (SiO_2) particles synthesized using the sol-gel Stöber method as a substrate for Ag deposition. This kind of SiO_2 is used because it is stable and the abundant silanol groups on the SiO_2 layers provide an active surface attachment for the various functional groups, for example, for easy deposition of Ag particles. Different methods have been developed for the deposition of Ag nanoparticles onto SiO_2 spheres. These techniques include a number of chemical reduction processes (Kalele et al., 2005; Ye et al., 2007; Flores et al., 2008) via either mechanical or ultrasonic irradiation. Other methods include the polyol process (Carotenuto, Pepe & Nicolais, 2000), nonionic reverse micelles (Zhang, Cheng & Ma, 2001), microwave irradiation (Pal, Shah & Devi, 2009) and ultraviolet photochemical deposition (Luo et al., 2009).

In order to expand the multifunctionality of Ag-SiO_2 hybrid composites, iron oxide nanoparticles such as magnetite or maghemite have been inserted into the core structures of the SiO_2 particles. They provide a hybrid material with a ferro- or superparamagnetic behavior. Such iron oxide-SiO_2-Ag coreshell composite powders can be applied, for example, as a recyclable surface-enhanced Raman scattering (SERS) material for melamine detection or as a nanoprobe for biomedical applications (Hu et al., 2010; Jun et al., 2010; Lv et al., 2010). Other possible applications include a magnetic disinfectant with enhanced stability and antimicrobial activity (Zhang et al., 2011). Only a few researchers have reported on the deposition of Ag onto an iron oxide-core SiO_2-shell surface in comparison to SiO_2-Ag structures. The synthesis methods that have been reported include reduction of Ag with glucose in a water bath (Hu et al., 2010), room temperature reduction with D(+)-lactose (Zhang et al., 2011) and deposition of Ag by electroless plating via ultrasonic route (Lv et al., 2010). In order to immobilize the Ag nanoparticles onto SiO_2 spheres or on the iron oxide-SiO_2 coreshell structures, most of the reported synthesis work required an additional surface functional modifying agent and various reducing agents such as thiols, sodium borohydride ($NaBH_4$), formaldehyde, or polyvinylpyrrolidone (Chou and Ren, 2000; Lee et al., 2007; Flores et al., 2008; Quang et al., 2011). Most of the synthesis of silver on silica surfaces reported in the literature reviewed here was conducted at elevated temperature or by reflux.

In this work, the immobilization of Ag nanoparticles on magnetite-silica surfaces is attempted using only PVP as a reducing agent in an ethanol solution at room temperature. Modification of the silica surface prior to the deposition of silver nanoparticles and additional reducing agent is eliminated. Thus this work promotes a simple and cost-saving route for deposition of Ag nanoparticles onto magnetite-silica coreshell structure surfaces.

1.4.2 Functionalization with silver/silver chloride particles

Silver chloride (AgCl) particles are known to be good candidates for photocatalytic activity, especially in water splitting and decomposition of organic compounds (Currao et al., 2004; Chen et al., 2012). These particles also exhibit a good antimicrobial property that can be used for the fabrication of antiseptic catheters, bone cements and fabrics (Adams, Santschi & Mellencamp, 1999). Furthermore, there has been interest recently in AgCl particles as important component materials for visible-light-driven photocatalysts (Wang et al., 2008; Choi et al., 2010; Kim et al., 2010; An et al., 2012; Chen et al., 2012). However, the AgCl particle only absorbs light in the ultraviolet range (180–380 nm) due to its semiconductor indirect band gaps of 5.15 eV (~240 nm) and 3.25 eV (~380 nm) (Gaus & Calzaferri, 2003). Thus by the nucleation of Ag nanoparticles on its surface, the absorption of this Ag/AgCl composite can be extended in the visible-light wavelength due to the surface plasmon resonance of Ag nanoparticles (400 nm), and it has become a good candidate for plasmonic photocatalyst applications. The combination of AgCl/Ag as a photocatalyst has been reported to be more stable than titania (Wang et al., 2008). Additional advantages of this hybrid material include a wide adsorption range in visible light (Wang et al., 2008; Choi, Shin & Jang, 2010; Kim et al., 2010) and higher efficiency in the decomposition of organic pollutants. Several researchers have reported on the preparation of Ag/AgCl composites for photocatalytic studies. Choi, Shin & Jang (2010) synthesized Ag/AgCl nanostructures by reacting silver nitrate ($AgNO_3$) with hydrochloric acid (HCl) using polyvinyl alcohol (PVA) as a dispersing agent followed by inducing the Ag nanoparticles on AgCl surfaces by light irradiation, while Kim et al. (2010) demonstrated the formation of AgCl nanocubes by controlling the molar ratio of the precursors: silver and chloride ions. In order to expand the functionality of these composites, e.g., catalyst recovery and reuse, An et al. (2012) constructed the magnetic visible-light-driven plasmonic Fe_3O_4@SiO_2@AgCl:Ag by a combination of polyol, sol-gel and photo-reduction methods. However, the synthesized AgCl structures were of micron size (bigger than the iron oxide-silica coreshell itself) since the growth of AgCl occurred rapidly and it did not seem easy to produce small particles.

Based on the literature, synthesized AgCl structures are of micron size and the formation of Ag nanoparticles on their surfaces was conducted either by chemical reduction or exposing to the light or heat irradiation. In addition, in author's knowledge only one report could be found on incorporating the magnetic core inside the micron-size AgCl particles acting as a mobile plasmonic photocatalyst (An et al., 2012). In this work, synthesis of the Ag/AgCl doped magnetite-silica coreshell structures is developed. The nano-sized AgCl particles are produced by controlling the concentrations of hydrochloric acid. In addition, a new method is developed for the synthesis of both Ag and AgCl particles simultaneously.

1.5. Compaction of nanopowders

Previous sections reviewed the unique properties of multifunctional nanopowders. Nevertheless, the novelty or enhancement of the properties of the nanopowders can also be found, when they are transformed into bulk composite materials by compaction or consolidation methods. For example, $MgAl_2O_4$ particulate, when consolidated (Wang & Zhao, 2009), can be transformed into a transparent bulk material with superb mechanical properties and high added-value applications such as airborne optics and as a transparent medium in hostile environments. Compaction of the materials is the process, where the initially weak porous body particles are converted into dense and strong bulk materials. The major purpose is to achieve nearly-full densification with minimal microstructural coarsening and undesirable microstructural transformations. For nanopowders, the densification process is quite challenging because grain growth and coarsening, insufficient interfacial bonding and remaining porosity may become a major problem. These factors affect most properties of the compacts and especially their mechanical properties. In addition, powder agglomeration, high reactivity of nanopowders, and possible contamination due to the high surface area of nanopowders also contribute to the inability to compact dense bulk materials. Thus major improvements have been made in overcoming these problems by developing the consolidation techniques.

A number of consolidation processes have been used in making dense compacts while aiming to retain the properties of the nanopowders (for example, the grain size). Traditionally, compaction processes rely on either conventional (pressureless) or non-conventional (pressure-assisted) sintering (Groza, 2007). In conventional sintering, the powder is first compacted as a green body followed by heating to sintering temperature, where the body is held until sintered (dwell time) and then cooled. This process is time consuming. In addition, undesirable side effects such as grain growth occur because of the hold at high temperature for a long time. Nevertheless, the introduction of pressure-assisted sintering in the compaction of nanopowders has improved the densification process with reduced grain growth compared to the pressureless sintering (Lange, 1989). This is due to the shear component of the applied stress that causes the collapse of the pores and rearrangement of the particles, which is beneficial for agglomerated powders. The capability to collapse the pores in pressure-assisted sintering scales with the shear stress level. This stress is minimal in hot isostatic pressing (HIP) and increases gradually from quasi-isostatic pressing to hot pressing (HP) to sinter-forging and finally extrusion. Nevertheless, more advanced sintering methods have been developed to improve the minimization of the grain growth when compacting the nanopowders, such as microwave sintering (Katz, Blake & Scherer, 1989;

Clark & Sutton, 1996) and electric current assisted sintering (ECAS). The basic idea of ECAS was first proposed in early 1920's by Duval d'Adrian (1922). In the following years, major improvements were made in developing the proposed idea (Taylor, 1933; Jones, 1940; Cremer, 1944; Ross, 1945; Inoue, 1966a; Inoue, 1966b; Inoue, 1967), and the work is still ongoing. Year by year, ECAS is increasingly recognized as pulsed electric current sintering (PECS), spark plasma sintering (SPS) or the field assisted sintering technique (FAST).

In PECS, the activation of sintering and densification is realized by charging a high pulsed electric current directly through the powders in a die under externally applied pressure. The PECS furnace is usually equipped with a vacuum chamber that allows the consolidation process to take place in a vacuum or in inert gas media such as nitrogen or argon. Typically the equipment is also supported by a computer-aided design system for temperature and pressure control inside the die.

In PECS, the consolidation process proceeds through two stages. In the first stage, a direct impulse current is used to initiate the sintering. The current also creates a magnetic field. The interaction of the field and the current is accompanied by radial compression of the powder. For conducting powders, the heating is by electro-resistive heating, while for non-conducting powders, the heating is by the thermal conductivity of the heated graphite matrix and pistons. In the second stage of consolidation, the pressure can be changed, depending on the sintered substance. Heat transfer from the graphite matrix/mold to the sintered powder is very effective as the graphite matrix itself serves as a heating element. The applied heating rate is usually high, typically from 100 to 400 K min^{-1} or even higher (up to 1000 K min^{-1}), and the dwell time is short (typically a few minutes). It is possible to obtain compacts with a density close to the theoretical density value at relatively low temperatures, even several hundred degrees lower than for the conventional hot pressing (Raguya, 2010). A schematic diagram of PECS is shown in Fig. 1.4.

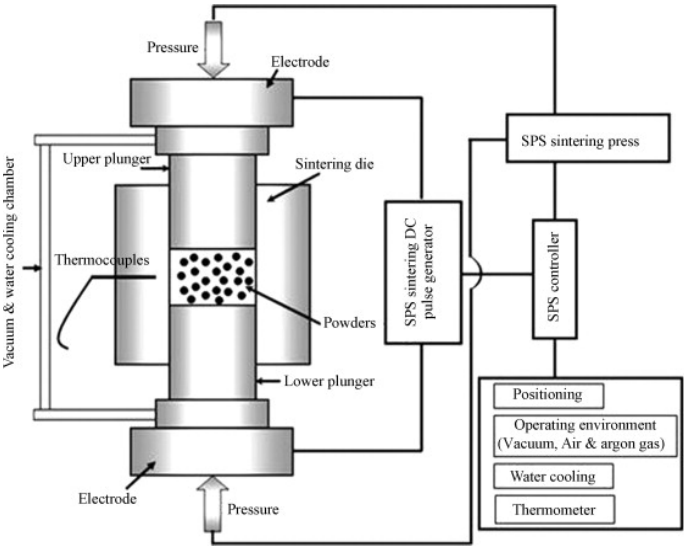

Fig. 1.4 Schematic diagram of pulsed electric current sintering. Reprinted from Dong et al. (2008) with permission from Elsevier.

1.5.1 Pulsed electric current sintering compacts and their properties

Compaction or consolidation of nanocomposites by PECS has attracted much attention due to the near-full densification, with the density close to the theoretical value of the components. As described above, this method also applies shorter processing times as well as rapid heating and cooling that contribute to inhibition of the grain growth during the sintering, thus maintaining the fine crystallite size of the nanopowders. Another impressive advantage of PECS is that it can be used in sintering of various types of powders, such as ceramics (Wang & Zhao, 2009; Ran et al., 2010), conductors (Yoon et al., 2011), semiconductors (Yu et al., 2012), amorphous alloys (Kim et al., 2007) and polymers (Omori et al., 1997), or materials that are not applicable for any other consolidation techniques. For example, Ran et al. (2010) showed that the PECS method is a very efficient technique for producing a dense nanostructure CuO doped 3Y-TZP ceramic with 70 nm grain size. In addition, the microstructure, i.e., grain size and phase composition of the CuO doped 3Y-TZP nano-ceramics, could be manipulated to a large extent by combining PECS with other processing techniques, including pressureless sintering and subsequent annealing. Limitation of grain growth and fast and maximum densification are also useful properties in producing transparent bulk materials. This has been demonstrated by Wang and Zhao (2009), for example, who showed the feasibility of using PECS in the fabrication of high quality, fine-grained, transparent spinel ceramics without any sintering aids.

Besides compaction of ceramics, semiconductors, amorphous alloys and so on, PECS has also received great attention for consolidation of magnetic materials such as cobalt ferrite nanopowders (Millot et al., 2007), which exhibit high coercivity and strong magnetic anisotropy. With these properties, cobalt ferrite has become an interesting material for permanent magnet and high-density recording applications. In order to keep the powder properties in a bulk material, phase transformations and grain growth should be avoided while obtaining a dense microstructure, since the magnetic properties of the material depend on the cation distribution, oxidation degree and crystallite size. Millot et al. (2007) have shown that by using PECS, a pure spinel phase with theoretical cationic distribution can be obtained when compacting cobalt ferrite nanopowders. In addition, no grain growth was observed at a significant densification of 91%. Bousnina et al. (2010) consolidated nickel nanopowders by using PECS and HIP and compared the obtained properties with commercial bulk nickel. The smallest grain size and the maximum strength and hardness were obtained for the PECS compacted powder, although the density of the compact was about 14% lower than bulk and comparable to the density obtained by HIP. It was found that SPS limits the increase of the grain size. Other magnetic materials that have been consolidated by PECS include Fe-Co soft magnets and FePd alloy (Nicula et al., 2007; Saravanan et al., 2010). Most of them aim to obtain a dense compact, controlled crystallite size, higher mechanical properties, etc.

However, there are no reports on PECS fabrication of transparent magnetic materials. Iron oxide nanoparticles such as magnetite (Fe_3O_4), maghemite (γ-Fe_2O_3) and pure iron are known to exhibit high saturation magnetization values (Guardia et al., 2007; Kura, Takahashi & Ogawa, 2010). When they are combined with transparent matrix materials, the composites can attain novel properties and potentially be used in applications based on their magnetic and optical properties. One of the properties that has attracted much attention in recent research is the magneto-optical effect applied in magneto-optical switches, information storage, optical fiber sensors, optical isolators, etc. (Krumme et al., 1977; Bahuguna et al., 2006; Zamani, Ghanaatshoar & Alisafaee, 2011).

Several studies deal with preparing transparent magnetic material based on iron oxide particles by using a variety of transparent matrices. Yamaguchi, Matsumoto & Fuji (1990) synthesized the transparent magnetic thin films by embedding Fe_3O_4 nanoparticles into the polyvinyl alcohol (PVA) matrix. However, due to the thermal and chemical instability of the polymer, the silica (SiO_2) matrix has received increasing interest. Yasumori et al. (2000) produced a transparent silica gel layer with embedded magnetite nanoparticles by using a sol-gel method, and Thomas et al. (2006) reported on crack-free transparent magnetic-silica monoliths in which the magnetite nanoparticles with various concentrations were entrapped within a sol-gel silica network formed in heat treatment. The magnetic and transparency behavior of both types of samples were found to depend on the iron oxide concentrations. However, there are apparently no reports on sintering of the bulk transparent magnetic material made of the amorphous silica powders with magnetite nanoparticle cores using the PECS method. Mayerhöfer et al. (2008) used PECS to compact a transparent glass from commercial silica nanopowders, which were not fabricated via the Stöber method. In this thesis, compaction of magnetite-silica coreshell powders by PECS represents a new exploration of the properties of the compacts. In addition, the silver-doped magnetite-silica coreshell structure is also compacted and the influence of silver doping on the properties of magnetite-silica compact is investigated.

1.6 Aim of the research and steps in reaching the goal

The purpose of this research is to develop a novel multifunctional magnetic core carrier material suitable for a variety of potential applications utilizing coreshell structures. This material should be adaptable to various surface modifications that are useful in powder or bulk form.

The work is based on the synthesis of magnetite-core materials followed by an amorphous silica coating as a shell. Further development of the magnetic-core with silica-shell structure can be divided into two parts: 1) functionalization of the coreshell powders with noble metal species and 2) compaction of the synthesized hybrid coreshell powders by PECS. The research tasks for achieving this were:

Task 1: Development of chemical synthesis of magnetite-core nanoparticles based on reverse co-precipitation
Task 2: Application of the Stöber method for the coating of synthesized magnetite nanoparticles with amorphous silica layer in the form of coreshell structures
Task 3: Functionalization of the silver nanoparticles onto the surfaces of magnetite-silica coreshell powders by wet chemistry methods
Task 4: Functionalization of the silver chloride nanoparticles onto the surfaces of magnetite-silica coreshell powders by wet chemistry methods
Task 5: Compaction of magnetite-silica coreshell powders for magnetic transparent bulk material utilizing the PECS method
Task 6: Compaction of different types of functionalized coreshell powders by PECS at different temperatures

In **Task 1**, the focus was on investigating the properties of the magnetite-core nanoparticles synthesized in ambient atmosphere by using various concentrations of ion ferrous salt. Since it was found that the synthesized magnetite was partially oxidized, which affected its magnetic properties, **Task 2** was applied to control the oxidation and thereby improve the magnetic properties of the magnetite. In addition, an amorphous silica-shell was formed to provide an active surface for further functionalization of the coreshell powders. **Task 3** described further functionalization of the magnetite-silica coreshell structures by introducing silver nanoparticles onto the surface of the coreshell powders. The focus of this work was to promote a simple and cost-saving route for the deposition of Ag nanoparticles onto magnetite-silica coreshell structures. As it was also found that the existence of silver chloride together with silver particles can expand the functions of hybrid magnetite-silica-silver composite, **Task 4** was directed at synthesizing the silver chloride particles onto the coreshell surfaces by inducing the hydrochloric acid. The aim was to produce a very small size AgCl (nanometer scale) to be attached on the surface of a silica structure by controlling the concentration of chloride ion source. Since the larger surface area provides more adsorption capacity, this work may provide some further knowledge on preparing nanosize AgCl particles with larger surface area to increase the efficiency of plasmonic photocatalyst activity.

In **Tasks 5** and **6**, different approaches were used to study the compaction of synthesized powders and the properties of the compacts. The prepared magnetite-silica coreshell powders were compacted using PECS. The focus of this approach was to investigate the interesting new properties that can be obtained when coreshell nanocomposite powders are transferred into bulk composite materials. In **Task 5**, the main objective was to produce a transparent bulk magnetic compact with potential application in magneto-optics. Since it was found that reduction of magnetite inside the silica shell occurred during compaction, **Task 6** was applied to investigate the reducing environment that was created during the compaction together with the optimum reduction temperature involved during the PECS. The combined influence of the temperature and atmosphere on the phase transformations of the magnetic-core and the silica-shell is important to know for any applications involving further processing of the coreshell powders. All the applied tasks are summarized in Publications I–VII.

2. Experimental

2.1 Starting materials and chemicals

The reagents that were applied during the experiments were ferrous sulfate ($FeSO_4 \cdot 7H_2O$, Merck), ammonium hydroxide 24.5% (NH_4OH, J.T. Baker), tetraethyl orthosilicate 98% (TEOS, Acros), ethanol 96% (EtOH, Altia), silver nitrate ($AgNO_3$, Sigma-Aldrich), polyvinylpyrrolidone (PVP, m.w. 10 000, Sigma-Aldrich), hydrochloric acid, 37–38% (HCl, J.T. Baker), dimethyl sulfoxide (DMSO, Sigma-Aldrich) and deionized water. All the materials were used as-received without further purification. The synthesis of the iron oxide nanoparticles followed by their functionalization with the SiO_2 layer and doping with Ag and AgCl particles and the PECS compaction process are described in the sections below.

2.2 Particle synthesis

2.2.1 Synthesis of magnetite nanoparticles

A reversed chemical co-precipitation method was applied in preparing the magnetite nanoparticles. In the synthesis, $FeSO_4 \cdot 7H_2O$ was used as a magnetite precursor with NH_4OH solution as a precipitating agent. Two synthesis protocols were applied during the precipitation process. For Synthesis Protocol 1 (SP1), 10 ml of iron ion (II), Fe^{2+}, was added drop-wise every 10 minutes to the magnetically stirred base solution. After the last addition, the mixed solution was allowed to react under constant stirring for 1 hour followed by overnight ageing. In Synthesis Protocol 2 (SP2), the Fe^{2+} was added at once to the base solution, mixed for 1 hour, and washed immediately. The black solution was then washed and dried in an ambient atmosphere oven at 323 K. The dried powder was ground using a mortar. Details of the process can be found in Publication I.

In Publications II–VII, the preparation of magnetite nanoparticles followed one of the methods described above. Details of the process are explained in each publication.

2.2.2 Synthesis of magnetite-silica coreshell structures

The synthesis of the magnetite-silica coreshell particles in Publications II–IV was based on the modified Stöber method (Lu et al., 2008). TEOS and an ethanol solution were mixed using mechanical stirring. Ammonium hydroxide, which catalyzes the formation of primary silica, was added to the mixture. A certain amount of magnetite powder was dispersed in the deionized water under ultrasonication. The magnetite solution was then added to the mixture in the intermediate process of hydrolysis and condensation of TEOS. During this stage the preformed primary silica nanoparticles aggregated with the magnetite nanoparticles due to their chemical surface affinity and formed the coreshell structures.

In Publications V–VII, where a larger amount of coreshell powder was needed for the PECS compaction, a modification was made in the consecution of adding the chemicals and materials during the Stöber process. In Publication V, the addition of TEOS was done twice in the middle and last steps of the process while in Publications VI and VII, the TEOS and NH_4OH were added in the last step of the process. These modifications were made in order to prevent the rapid hydrolysis and condensation of TEOS during the process due to the larger amount of catalyst and precursor used, which can result in the formation of magnetite-free silica particles.

2.2.3 Silver-doping of magnetite-silica coreshell structures

The preparation of the magnetite-silica coreshell powder follows the method described in Section 2.2.2. The depositions of Ag nanoparticles onto the silica surfaces were conducted using four different approaches.

In *Approach 1*, $AgNO_3$ powder was dissolved into the deionized water for a certain concentration. Then the Ag^+-containing solution was added to the prepared magnetite-silica solution. The solution was mechanically stirred to ensure the absorption of Ag^+ species on silica surfaces. For reduction of Ag^+ into Ag, PVP was used as a reducing agent. This PVP was dispersed in ethanol and added to the Ag^+-containing solution, stirred and aged.

In *Approach 2,* Ag^+ was reduced in an ethanol-PVP solution to form Ag atoms in the form of Ag colloids. This mixture was then poured into the magnetite-silica solution, followed by mixing and aging.

In *Approach 3,* a similar synthesis method as in Approach 1 was utilized, except for the preparation of the magnetite-coreshell powders prior to the Ag^+ adsorption process.

In *Approach 4,* the absorption of Ag^+ and reduction by PVP were conducted via ultrasonic method.

Details of these processes are described in Publication III.

The preparation of the magnetite-silica coreshell powder for PECS follows the method described in Section 2.2.2. After completion of the process of hydrolysis and condensation, forming the coreshell structure, $AgNO_3$ aqueous solution was added. Stirring of the mixture was continued for 2 hours to ensure the absorption of Ag^+ on the silica surface. The powder was dried naturally under a fume hood, ground and annealed prior to the PECS process [Publication VII].

2.2.4 Silver-/silver chloride-doping of magnetite-silica coreshell structures

The preparation of the magnetite-silica coreshell powder follows the method in Section 2.2.2. The absorption of Ag^+ follows Approach 1 in Section 2.2.3 except for the reduction with PVP. In a different beaker, about 0.3 ml of HCl was injected into the ethanol-PVP mixture, followed by the addition of as-prepared Ag^+-rich magnetite-silica coreshell solution. The ultrasonic mixing was done for 1 hour and the sample was aged overnight without mixing. The sample was then washed with deionized water for the removal of excess PVP by a centrifuge, dried in an oven at 333 K and ground. The synthesis process was repeated by using different concentrations of HCl. Details of the experiment are described in Publication IV.

2.3 Pulsed electric current sintering of hybrid coreshell powders

PECS experiments were carried out using FCT HPD 25-2 equipment (FCT Systeme GmbH). The coreshell composite powder was placed in a graphite mold with an inner diameter of 20.8 mm. The inner surface of the mold was covered by graphite foil with 0.4 mm thickness in order to increase the surface contact. In each compaction about 2.2–2.6 g of the powder was used. The sintering temperature was varied from 873 K up to 1373 K. Sintering was carried out for 15–30 min in a vacuum of 9–15 Pa by applying axial pressure of 50 MPa. The heating rate used was 373 K/min. The thickness of the consolidated samples was in the range 2–5 mm. After the sintering, the surface of the compacts was ground using SiC paper up to 1200 mesh prior to their characterization. Details on the preparation of the powders and PECS process parameters are described in Publications V–VII.

2.4 Characterization of materials

2.4.1 Phase determination

The phase composition of the synthesized particles and compacts [Publications I–VII] was determined using X-ray diffraction (XRD Philips PW1710) over a 2θ range 10°–90° using CuK$_\alpha$ (λ=1.5046). Analysis of XRD patterns was carried out using X'Pert HighScore Plus Software incorporating ICCD PDF-4 files (version 2009–2012). The refinement of the powder pattern in Publication I was conducted using PowderCell 2.4 software. In Publication II, Mössbauer spectroscopy in the transmission mode was used to determine oxidation behavior and the magnetic phase in the sample. The Mössbauer spectra measurement was carried out in the transmission mode with ^{57}Co diffused into an Rh matrix as a source moving with constant acceleration at room and helium temperatures. The spectrometer (Wissel) was calibrated using a standard α Fe foil, and the isomer shift was expressed with respect to this standard at 293 K. The fitting of the spectra was performed with the help of the CONFIT program. The selected-area-electron-diffraction patterns (SAEDP) of the Ag/AgCl doped magnetite-silica coreshell particles in Publication IV were obtained using a transmission electron microscope (TEM Tecnai F20) operated at 200 kV to confirm the phase structures.

2.4.2 Crystallite size measurement

The crystallite size of the synthesized particles [Publications I–VII] was estimated using Scherrer's equation (Cullity & Stock, 2001), given as follows (Eq. 2.1.):

$$t = \frac{0.9\lambda}{B\cos\theta_B} \qquad (2.1)$$

where

t = estimate of the crystallite size,

B = full-width-half-maximum (FWHM),

λ = X-ray wavelength of the source material, and
θ_B = Bragg angle.

B refers to the spectral breadth or broadening due to the crystallite-size effect. For the calculation, the B value must be the net value of B of the reference sample (B_{ref}) and B of the observed sample (B_{obs}), with $B = B_{obs} - B_{ref}$. As an example, for the crystallite size calculation for synthesized magnetite nanoparticles, the commercial magnetite powder (ref) was used for the B_{ref}.

2.4.3 Microscopy studies

Microscopy studies were conducted by using different microscopic techniques. In Publications I–V and VII, the morphology observation of the synthesized particles was conducted using a TEM Tecnai F20 operated at 200 kV. For the particle size calculation, Digital Micrograph software was used. For the high-resolution TEM images in Publication III, an aberration/corrected high-resolution TEM JEOL JEM-2200FS operated at 200 kV was used. The high-angle annular dark-field (HAADF) scanning transmission electron microscope (STEM) was used to differentiate the phase structures of iron oxide-core, SiO_2-shell and Ag- or Ag/AgCl-doped nanoparticles in Publication III, with the association of energy dispersive spectroscopy (TEM-EDS). A scanning electron microscope with energy dispersive spectroscopy (SEM-EDS Hitachi S-4700) was used to observe the morphology and particle size of the AgCl-doped coreshell surfaces in Publication IV.

In TEM sample preparation, a small amount of the powder was dispersed in ethanol under ultrasonic mixing for 3 minutes. Then 6.7 microliters (μL) of the dispersed solution was dropped on a carbon- or fomvar-coated copper grid and left for 2 hours for drying prior to microscopic analysis.

The fractured and polished surfaces of the PECS compacts presented in Publications V and VII were studied using an SEM-EDS Hitachi S-4700.

2.4.4 Magnetic measurement

Magnetic properties of prepared powders at temperatures from 800 K to 10 K were evaluated using vibrating sample magnetometers (VSM). The magnetization curves or hysteresis loops at room temperature were measured by VSM PAR–Lakeshore in the field up to 1.4 T. The temperature dependence of magnetization and magnetization curves at higher magnetic fields up to 9 T was determined using a VSM insert in the Physical Property Measurement System (PPMS) by Quantum Design. The measurement of the temperature dependence of magnetization at 100 Oe and in saturation was used to evaluate possible phase transformation of the magnetic samples.

For the powder sample preparation, about 10 mg of the powder was wrapped in aluminum foil. This wrapping was then attached to the VSM holder and measured. The sintered samples were prepared by cutting a bar of the bulk compacted disc about 2 mm wide. The bar was then measured in a similar way as the powder sample.

2.4.5 Thermal behavior

The thermal behavior of the powder samples was studied using differential scanning calorimetry (DSC) and thermo gravimetric analysis (TGA) (Netzsch STA 449 C Jupiter DSC/TGA) [Publication VI]. A few milligrams of the powder was placed in the alumina crucible. The measurement was conducted in an argon atmosphere at 283 K/min heating rate. The maximum temperature used was 1323 K.

2.4.6 Optical studies

The absorption of the Ag/AgCl-containing solution [Publications III and IV] in the UV-visible range 250–800 nm was studied using a UV-visible spectrometer (Perkin Elmer Lambda 950). For the sample preparation, about 5 milligrams (mg) of the powder was dispersed in 10 milliliters (ml) of either ethanol or DMSO solution. The dispersed solution was placed in a plastic cuvette for the measurement.

The transparency of the compacted samples in Publication V was studied using a similar spectrometer as above, with total transmission mode over the wavelength range of 250–800 nm.

2.4.7 Density measurement

The density measurement was applied to the PEC sintered samples using an Archimedes method (Sartorius CPA224S, 0.1 mg). The measurement was conducted in deionized water. In Publication V, the density value was used in determining the molar volume (V_m) of the compacted sample using Eq. 2.2:

$$V_m = \frac{M_T \text{ x } mole\ fraction}{\rho} \qquad (2.2)$$

where M_T is equal to the total molar mass of the components. This value has been used to indicate the structural changes in the glass network of the compact. In Publication VII, the density measurement was used to estimate the relative densities of the hybrid compacts. In order to take into account the influence of open porosity a thin layer of bee wax was introduced to the surface of the sample. The rule of mixture was used in the calculation of theoretical density of the compact as follows (German & Park, 2008):

$$\frac{1}{\rho_T} = \frac{W_{P1}}{\rho_{P1}} + \frac{W_{P2}}{\rho_{P2}} \qquad (2.3)$$

where

ρ_T = theoretical density of the mixture

W_P = weight fraction of the powder

ρ_P = theoretical density of the powder

3. Summary of Results

This chapter summarizes major findings of the research work. Details of the results can be found in the attached Publications I–VII.

3.1 Synthesis of magnetite-core nanoparticles

Magnetite nanoparticles have been used as a core material in Publications II–VII. In Publication I, research focused on the synthesis of magnetite-core nanoparticles using different concentrations of ferrous ions (Fe^{2+}) as a magnetite precursor, with an alkaline solution as a precipitating agent. Two different synthesis protocols were studied (SP1 and SP2), and it was found that the applied synthesis protocols affected the stoichiometries, crystallite and particle sizes, morphologies and magnetic behavior of the particles.

The XRD patterns were used in determining the stoichiometry of the synthesized magnetite powder. Refinement of the unit cell length, a, was made using the PowderCell 2.4 software. Gorski and Scherer (2010) derived the unit cell length of magnetite nanoparticles from the fitted powder XRD patterns of varying stoichiometries. Based on the given data, a linear interpolation was made for the Fe^{2+}/Fe^{3+} ratio, x, and the unit cell length, a, obeying the equation [Publication I]:

$$a = 8.34134 + 0.10512\,x \qquad (3.1)$$

This equation was used in estimating the stoichiometry deviation, δ, of the synthesized nanoparticles, which was later used in determining the chemical composition of the particles. Results are summarized in Table 3.1.

According to the results, the SP2 powders had stoichiometry approaching that of magnetite as the concentration of Fe^{2+} increased. In SP1, lower ferrous ion concentrations of 0.05 and 0.1 M resulted in strongly oxidized magnetite ($Fe_{2.78}O_4$, $Fe_{2.80}O_4$) that approached the maghemite stoichiometry, $Fe_{2.67}O_4$. The crystallite size was calculated using the Scherrer equation, while the particle size was calculated based on the TEM micrographs. The measured crystallite sizes were congruent with the particle sizes from the TEM measurements [Publication I, Fig. 2]. In SP1, the particle size distribution was relatively narrow, i.e., 8–22 nm, and quite similar for all the Fe^{2+} concentrations used. In SP2, the particle size distribution was wider (9–36 nm), and the particle size increased with the increasing Fe^{2+} concentration.

Table 3.1 Properties of synthesized magnetite based on two synthesis protocols [Publication I]

Fe^{2+} [M]	**Unit Cell Length, a (Å)**		**$Fe_{3-\delta}O_4$**	
	SP1	**SP2**	**SP1**	**SP2**
0.05	8.3565	8.3658	$Fe_{2.78}O_4$	$Fe_{2.85}O_4$
0.10	8.3582	8.3663	$Fe_{2.8}O_4$	$Fe_{2.85}O_4$
0.20	8.3627	8.3680	$Fe_{2.83}O_4$	$Fe_{2.86}O_4$
0.30	8.3614	8.3736	$Fe_{2.82}O_4$	$Fe_{2.89}O_4$
0.40	8.3738	8.3723	$Fe_{2.89}O_4$	$Fe_{2.89}O_4$
0.60	8.3715	8.3751	$Fe_{2.88}O_4$	$Fe_{2.90}O_4$
0.80	8.3660	-	$Fe_{2.85}O_4$	-
1.00	8.3612	-	$Fe_{2.83}O_4$	-

The morphologies of the synthesized magnetite nanoparticles for both synthesis protocols are illustrated in Fig. 3.1. Particles in SP1 are almost spherical in shape. In SP2, only the low concentration of Fe^{2+}, which is 0.2 M, showed similar morphology to SP1 particles. In SP2, as the Fe^{2+} concentration increased, the irregular, hexagonal morphologies appeared.

The agglomeration of the particles could be observed in all the SP1 and SP2 powders.

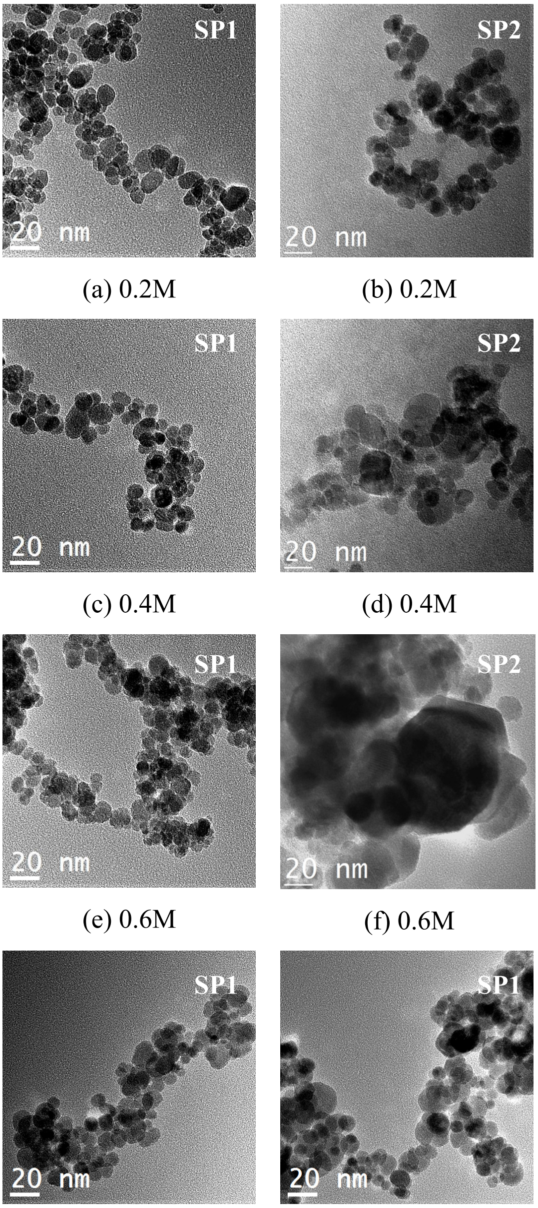

(a) 0.2M (b) 0.2M

(c) 0.4M (d) 0.4M

(e) 0.6M (f) 0.6M

(g) 0.8M (h) 1.0M

Fig. 3.1 TEM images of magnetic nanoparticles synthesized using various Fe^{2+} concentrations: SP1 [(a), (c), (e), (g) & (h)] and SP2 [(b), (d) & (f)] [Publication I]

Fig. 3.2 summarizes the room temperature magnetic properties of both SP1 and SP2 powders. In SP1 powders, the saturation magnetization increased when the particle composition approached magnetite, with decreasing crystallite size. However, this correlation does not hold for the SP2 powders. Although the SP2-0.6M had composition closest to magnetite, its saturation magnetization was the lowest.

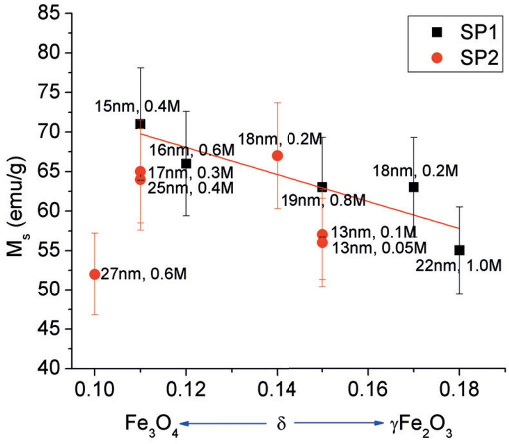

Fig. 3.2 Saturation magnetization of the synthesized magnetite ($Fe_{3-\delta}O_4$) powders as a function of δ [Publication I]

In Publication II, the magnetic behavior of the most oxidized magnetite nanoparticles from SP2 ($Fe_{2.85}O_4$) that were synthesized in Publication I was analyzed using low temperature magnetic measurements. Results showed that the saturation magnetization values increased at low temperature (10 K), showing the characteristics of a particular ferromagnetic behavior with the coercivity values pointing to the onset of superparamagnetic behavior. The calculated Curie temperature (T_C) based on the relative magnetization curve was about 800 K, which is close to that of pure bulk magnetite, 850 K (Cornell & Schwertmann, 2003). On the zero field susceptibility curve (Publication II, Fig. 3b) there is no sharp peak but only a shallow maximum at the Verwey transition temperature, T_V, which in bulk magnetite occurs at about 120 K (Verwey, 1939).

3.2 Stöber silica-shell

In Publications II–VII a modified Stöber method was used in forming the magnetite-silica coreshell structures. As observed from TEM images in Fig. 3.3, the synthesized magnetite-silica composite exhibited a perfect coreshell structure, where the magnetite nanoparticles were successfully coated with the silica-shell, and no magnetite residuals could be observed outside the shells [Publication II]. The average diameter of silica was about 50–150 nm. Coating with silica can prevent the agglomeration of the magnetite powder, when compared to the bare magnetite in Fig. 3.1 [Publication I].

The magnetization curves of magnetite-silica coreshell structure are shown in Fig. 3.4a. The saturation magnetization of the magnetite-silica coreshell powders exhibited the same trend as bare magnetite powders [Publication II], i.e., the M_S value slightly increased at lower temperature. The coercive force is nearly zero at room temperature, which indicates closeness to the superparamagnetic regime, but increases to a relatively high value of 0.03 T at 10 K. Based on the DC susceptibility measured from 350 to 10 K in Fig. 3.4b, there are not any pronounced changes, which would be a clear indication of the Verwey transition. Nevertheless, there is a broad peak around the temperature where the transition is expected. The broadness of the transition can be ascribed to the small size of the particles and their distribution. The estimation of the Curie temperature from the measurement at 10 K, 300 K and 800 K gives a rough value of 850 K.

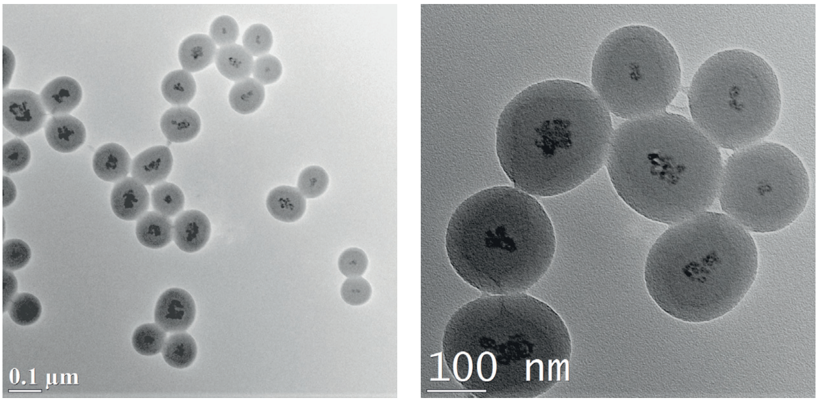

(a) (b)

Fig. 3.3 TEM images of magnetite-silica coreshell structures [Publication II]

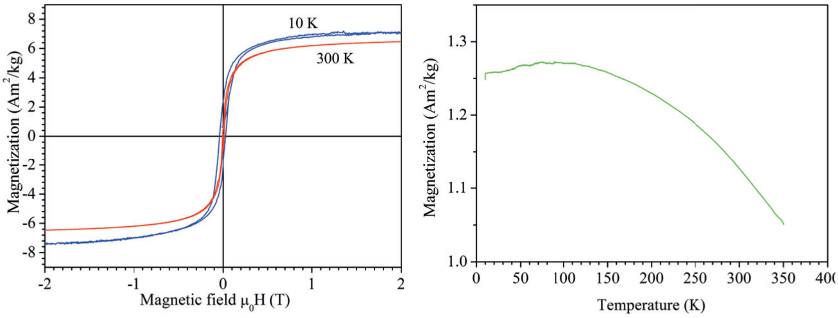

(a) (b)

Fig. 3.4 (a) Magnetization curves of magnetite-silica coreshell powders, and (b) low field magnetization at 100 Oe measured from high temperature down [Publication II]

3.3 Functionalization of the magnetite-silica coreshell powder

The magnetite-silica coreshell powders that were synthesized according to the method developed in Publication II were functionalized with noble metal species, i.e., silver nanoparticles. In Publication III, four approaches were studied for the silver-doping process. Common to the approaches was the use of PVP as a reducing agent for Ag^+. In Approaches 1, 3 and 4, the immobilization of Ag nanoparticles onto the surfaces of magnetite-silica coreshell structures was obtained through the reduction of Ag ions (Ag^+) on OH^- terminated silica-shell. A different method was applied in Approach 2, where the Ag^+ ions were not absorbed onto the silica surface but reduced in the ethanol-PVP solutions as Ag atoms/colloids. These Ag colloids were then mixed with the magnetite-silica solution. The role of PVP as a reducer was supported by the observed XRD patterns with distinct peaks of Ag in all the synthesis approaches used (Fig. 3.5). Additional peaks of AgCl were found in samples using Approaches 3 and 4 due to chlorine contamination during the synthesis. Magnetite phase was also observed for all samples.

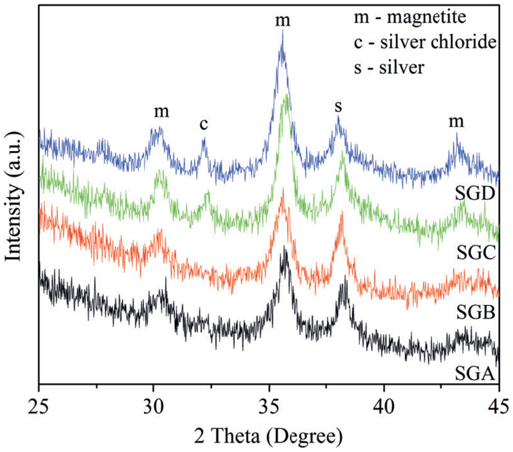

Fig. 3.5 The XRD patterns of the synthesized samples (SGA, Approach 1; SGB, Approach 2; SGC, Approach 3; and SGD, Approach 4) [Publication III]

TEM images in Fig. 3.6 show the evolution of the deposition of Ag nanoparticles onto the silica-shell surfaces as a function of time. In Approaches 1 and 2, silver nanoparticles had already started to grow on silica-shells after 30 min of reaction, and their amount increased with increasing process time (Fig. 3.6a–f). The remarkably large Ag nanoparticles (~41 nm on average) in Fig. 3.6d are assumed to have formed in the aggregation of the particles during the reduction process. In Approach

3, large particles (~20–50 nm) existed already after 30 minutes of synthesis (Fig. 3.6g), while the small-sized particles on the silica-shells were about 1 nm, in contrast to Approaches 1 and 2, where they were already ~5 nm in size (Figs. 3.6a and d). This size difference might result from Ag^+ favoring reaction with the chloride ions instead of forming Ag agglomerates. The suggestion is supported by the fact that the deposition rate of Ag and AgCl particles was quite poor, even after 3 and 18 hours of synthesis (Figs 3.6h and i), when compared to that observed in Approach 1. Nevertheless, the ultrasonic mixing in Approach 4 enhanced the particle formation after 30 min of reaction (Fig. 3.6j). Contrary to Approach 3, as the reaction time increased to 3 hours, additional nucleation of Ag/AgCl had occurred (Fig. 3.6k) and had become obvious after 18 hours (Fig. 3.6l). It can also be observed in Fig. 3.6 that the morphology of Ag-doped nanoparticles was spherical for all the synthesis approaches used. The individual deposition of Ag could be clearly seen without agglomeration, indicating that PVP could also act as a capping agent that prevents the agglomeration and controls the growth of Ag nanoparticles. However, irregular morphology could be observed in AgCl-contaminated samples.

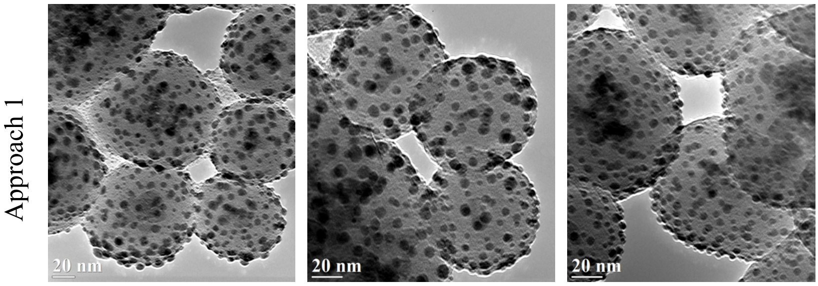

(a) 30 min (b) 3 h (c) 18 h

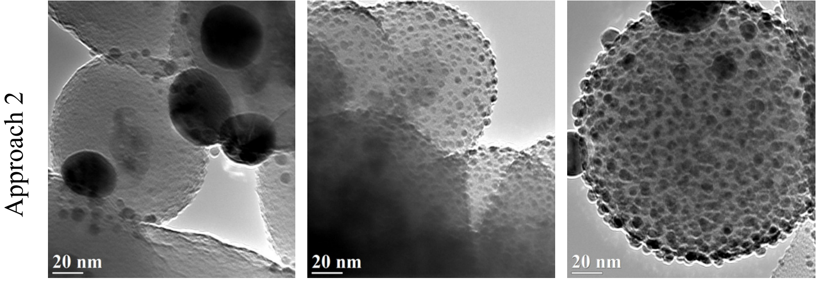

(d) 30 min (e) 3 h (f) 18 h

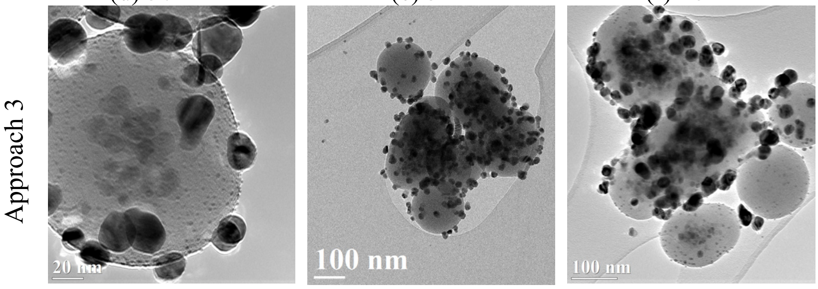

(g) 30 min (h) 3 h (i) 18 h

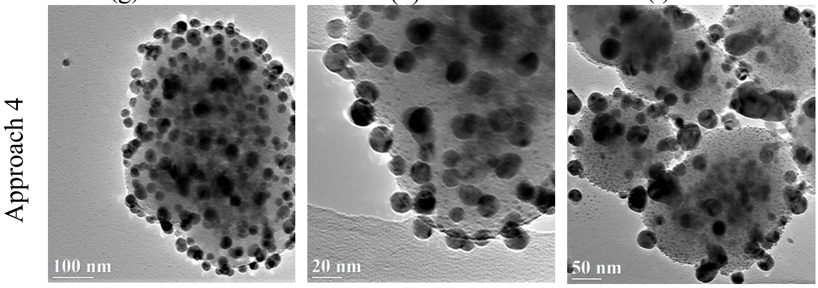

(j) 30 min (k) 3 h (l) 18 h

Fig 3.6 The evolution of Ag nanoparticle deposition on silica-shells as a function of time for all synthesis approaches [Publication III]

Table 3.2 gives a summary of particle size distributions for all samples as a function of time. Approach 1 gave the narrowest size distribution with the average particle size slightly decreased after 18 hours of ageing from about

9 nm to 5 nm. The decrease in particle size due to the formation of smaller Ag clusters as the reaction time increased indicates that the continuous reduction of silver ions by PVP has occurred. Approach 2 showed similar trends to Approach 1, while in Approach 3, the particle size remained stable even after 18 hours of synthesis due to the slow deposition rate of the Ag/AgCl particles. The size of particles in Approach 4 after 30 minutes was 15 nm on average, obviously due to the rapid deposition of particles by ultrasonic force. As the reaction time increased, the particles grew bigger, probably due to the formation of more AgCl than the Ag deposition itself. The slight decrease in the particle size after 18 hours of synthesis also corresponded to the formation of smaller Ag/AgCl clusters on the silica surface (Fig. 3.6l).

Table 3.2 Particle size distributions of Ag-doped silica-shell as a function of time for all synthesis approaches [Publication III]

Approach	**Particle size (nm)**		
	30 min	**3 h**	**18 h**
1	9 ±8	7 ±3	5 ±1
2	14 ±11	13 ±10	9 ±8
3	24 ±13	22 ±12	21 ±13
4	15 ±6	21 ±15	20 ±16

The formation AgCl phase in Approaches 3 and 4, due to the contamination of the coreshell powders (prior to deposition of Ag nanoparticles) during their preparation under ambient atmosphere [Publication III] may not limit the ability of the hybrid composites. AgCl has some similar applications to pure Ag and promotes a slow release of Ag^+ for antimicrobial property (Choi et al., 2008). AgCl can also be used as a plasmonic photocatalyst in combination with Ag nanoparticles (Choi et al., 2010). Thus in Publication VI, deposition of AgCl nanoparticles on silica-shell was attempted by adding a certain amount of HCl. The mechanism of Ag^+ absorption on silica-shells was similar to that in Publication III. Four different concentrations of HCl were used to induce the formation of AgCl particles, with the PVP as a capping agent that controlled the growth and morphology of the particles. The effectiveness of the HCl concentrations in the AgCl formation was observed from the SEM and TEM images, Figs. 3.7 and 3.8.

In Fig. 3.7a, a very high Cl^- concentration, $12x10^3$ mM, caused a rapid growth of AgCl, which resulted in extensive agglomeration of the particles. When the Cl^- concentration was strongly reduced down to 12 mM, a cubic-like structure was observed (Fig 3.7b). In addition, smaller spherical particles are also found in TEM investigation (Fig. 3.7b, inset). As the Cl^- concentration was further reduced to 1.2 mM, spherical and irregular morphologies were observed in Fig. 3.7. For the lowest Cl^--concentration, i.e., 0.12 mM, small AgCl particles distributed on the silica surface were found (Fig. 3.8a). Based on the selected-area-electron-diffraction (SAED) pattern of the particles in Fig. 3.8b, Ag phase was also present.

Both functionalized magnetite-silica coreshell powders in Publications III and IV showed an absorption peak in the UV-visible spectral wavelength. For Ag-doped structures, strong absorbance peaks [Publication III, Fig. 13] attributed to the surface plasma excitation of Ag nanoparticles was observed around 400 nm. Peaks became broader for the AgCl-contaminated samples. In contrast to the results in Publication III, the existence of AgCl phase gave strong absorption in the UV region, with a slightly broadened absorbance peak in the visible region due to the presence of Ag nanoclusters [Publication IV, Fig. 5].

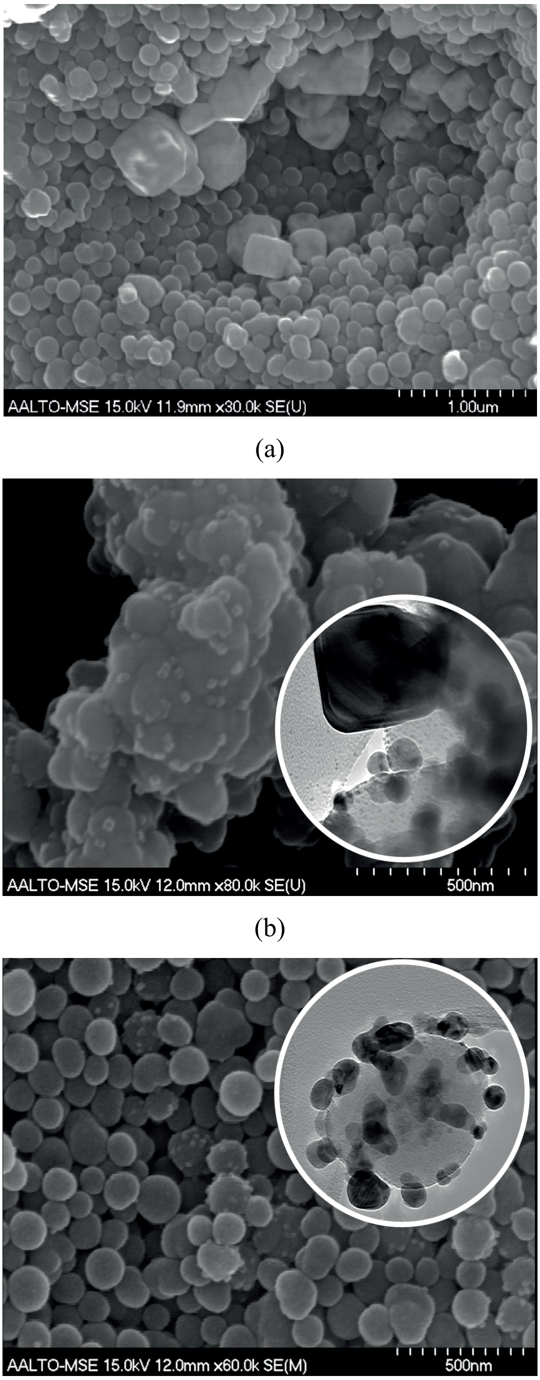

(a)

(b)

(c)

Fig. 3.7 SEM and TEM (inset) images of samples with different Cl^- concentrations: (a) $12x10^3$ mM, (b) 12 mM and (c) 1.2 mM [Publication IV]

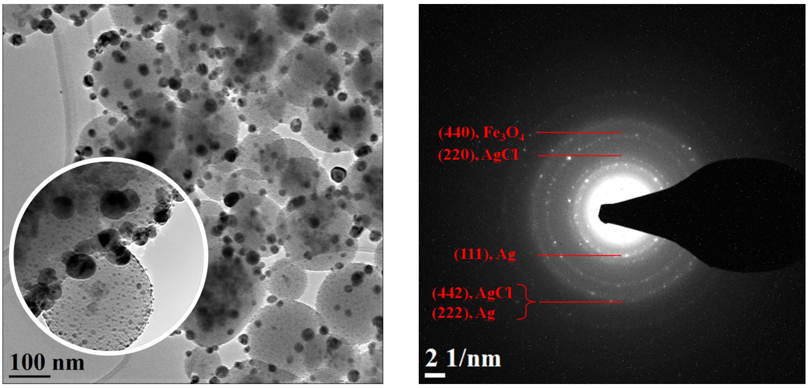

(a)

(b)

Fig. 3.8 (a) TEM image and (b) SAED pattern of sample with Cl^- concentration of 0.12 mM [Publication IV]

The saturation magnetization values for the functionalized magnetite-silica powders in Publication IV were for each sample 5 Am^2/kg on average. In Publication III, the saturation magnetization values were varied, depending on the synthesis approaches. Measured saturation magnetization of magnetite-core powder was about 70–74 Am^2/kg, which is in agreement with the value in Publication II. If similar amount of silica shell was assumed in all powders, the difference can be ascribed to different amounts of Ag or Ag/AgCl particles attached on the silica-shells. All powders with silver/silver chloride doping showed a ferromagnetic behavior at room temperature [Publications III and IV].

3.4 Pulsed electric current sintering of hybrid coreshell powders

In Publications III and IV, the magnetite-silica coreshell powders were functionalized with noble metal species. In Publications V–VII, compaction of these powders is explored in order to discover the interesting properties of bulk materials produced from magnetite-silica coreshell powders. PECS was used to compact the powders. By taking into consideration the size of synthesized magnetite that is smaller than the wavelength of visible light and the transparency properties of silica (Mayerhöfer et al., 2008), a transparent magnetic compact was targeted. Different amounts of magnetite nanoparticles were used to produce the magnetite-silica coreshell powders in order to study the influence of the magnetite content of the powders on the transparency of the final products [Publication V].

The transparency of the magnetic compact decreased and the compact became opaque when higher concentrations of magnetite were used. It was also found that the loss of transparency occurred with the phase transformation of the compacts [Publication V]. At zero and low concentrations of magnetite (0, 0.02 and 0.09 mol %), a transparent amorphous silica phase was obtained. Transparency was lost at the magnetite content of 0.18 mol %. Based on the SEM cross-section image of the compact (Fig. 3.9a), dendritic growth of crystals can be observed. These dendrites correspond to the crystallization of amorphous silica into quartz, as confirmed by XRD [Publication V, Fig. 2b]. The crystallization becomes extensive with columnar morphology (Fig. 3.9b) at the highest concentration of magnetite used (0.31 mol %), as supported by the full set of quartz peaks that appear in the XRD pattern of the compact. In addition, magnetite is reduced into pure iron, Fe. Based on these results, the magnetite content has a strong influence on the stability of amorphous silica during sintering, which finally affects the physical appearance of the samples after the consolidation process, as shown in Fig. 3.10.

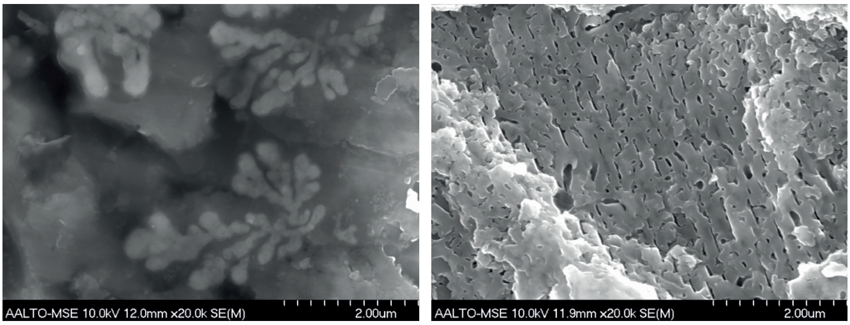

(a) (b)

Fig. 3.9 SEM cross-section images of fracture surfaces of compacts sintered at 1373 K. (a) 0.18 and (b) 0.31 mol % Fe_3O_4 [Publication V]

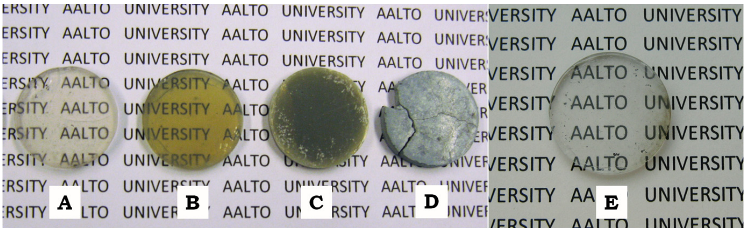

Fig. 3.10 The PECS compacted iron oxide-silica samples containing Fe_3O_4 (in mol %): (A) 0.02, (B) 0.09, (C) 0.18, (D) 0.31 and (E) 0 [Publication V]

The transformation inside the compacts was shown to depend on the magnetite content [Publication V]. However, the sintering atmosphere may also influence the phase transformations in the compact. This is explored in more detail in Publication VI. The investigation was done by comparing two different heating environments: PECS in vacuum and DSC/TGA in argon. Similar starting powders and temperature (1323 K) were used in both methods. Results are summarized in Table 3.3.

Table 3.3 Phase transformations of magnetite-silica coreshell structures after PECS and DSC

Sample	**Phase Formation**	
	PECS	**DSC**
magnetite	-	hematite
silica	amorphous	amorphous
0.05 g (magnetite-core)	α-Fe, quartz	hematite, magnetite, amorphous silica
0.10 g (magnetite-core)	α-Fe, quartz, cristobalite	hematite, magnetite, amorphous silica
0.15 g (magnetite-core)	α-Fe, quartz, cristobalite	hematite, magnetite, amorphous silica

Based on Table 3.3, the silica remains amorphous under PEC sintering and DSC analysis at 1323 K. Bare magnetite nanoparticles were used as a reference in DSC and this compound was transformed into hematite phase after heating. With silica-shells, hematite and magnetite phases were obtained and the amorphous phase of silica-shell retained. In PECS of all the magnetite-silica coreshell powders, α-Fe was formed and the amorphous silica-shell crystallized into quartz and cristobalite. The intensities of the quartz and cristobalite phases were enhanced with the increasing magnetite content (Fig. 3.11). These results show that the PECS atmosphere did have an influence on the properties of the final compacts. The correlation between the magnetite contents, sintering/heating environments and phase transformations in both Publications V and VII will be discussed in Chapter 4 (Section 4.3).

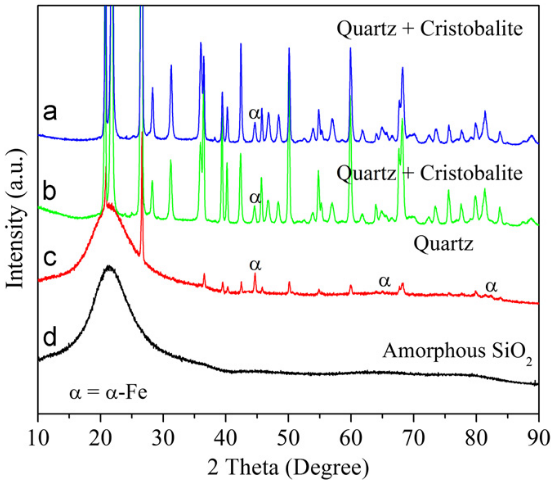

Fig. 3.11 XRD patterns of the PECS compacts sintered at 1322 K with different amounts of magnetite (a) 0.15, (b) 0.10, (c) 0.05 and (d) 0 grams [Publication VI]

It was also found that the reduction of iron oxide inside the silica shell was associated with the crystallization of amorphous silica at PECS temperature higher than 1273 K [Publications V and VII]. Therefore in Publication VII, the maximum temperature for sintering magnetite-silica (Batch A) coreshell powder during the PECS was studied in order to find the critical temperature for the phase transformations. Additional hybrid powders magnetite-silica-silver (Batch B) and silica-silver (Batch C) were also compacted to investigate the influence of silver nanoparticle functionalization on the PECS behavior of the powder compacts (Fig. 3.12).

The sintering temperatures were varied from 873 K to 1273 K. For magnetite-silica compacts, XRD patterns [Publication VII, Fig. 2b] of the compacts sintered at temperatures in the range of 873 to 1173 K showed only the magnetite and amorphous silica phases. The reduction of magnetite to α-Fe occurred at 1273 K concurrently with the crystallization of amorphous SiO_2 into quartz and cristobalite phases, in agreement with Publication V. Interestingly, different phase transformations occurred when Ag-containing starting powders were used (Batch B). Based on the XRD of the compacts, the magnetite was oxidized into hematite phase, and this oxidation became stronger at higher temperature. The formation of metallic Ag, which had already started during the annealing of the starting powder at 573 K, was enhanced as the compaction temperature increased. Silver oxides were found at sintering temperatures of 873 and 973 K and disappeared as the temperature increased [Publication VII]. Batch C compacts were used as a reference for Batch B. In the XRD patterns [Publication VII, Figs. 2c and d], Ag peaks similar to those in Batch B were observed for all compacted samples. However, silver might have started to melt both in Batch B and C compacts at 1173 K, which is close to the melting temperature of silver (1233 K).

The room-temperature magnetization of the ferromagnetic coreshell powders changed after PECS compaction [Publications V and VII]. In Publication V, diamagnetic and paramagnetic behaviors were found in the transparent and translucent compacts, while ferromagnetism was observed for the non-transparent compacts [Publications V and VII]. It was found that the saturation magnetization values of the compacts were higher than in the starting powders if the magnetite phase remained after the compaction [Publication V]. In contrast, the M_S values of the compacts were lower when reduction or oxidation of the magnetite phase in the compacts occurred [Publications V and VII].

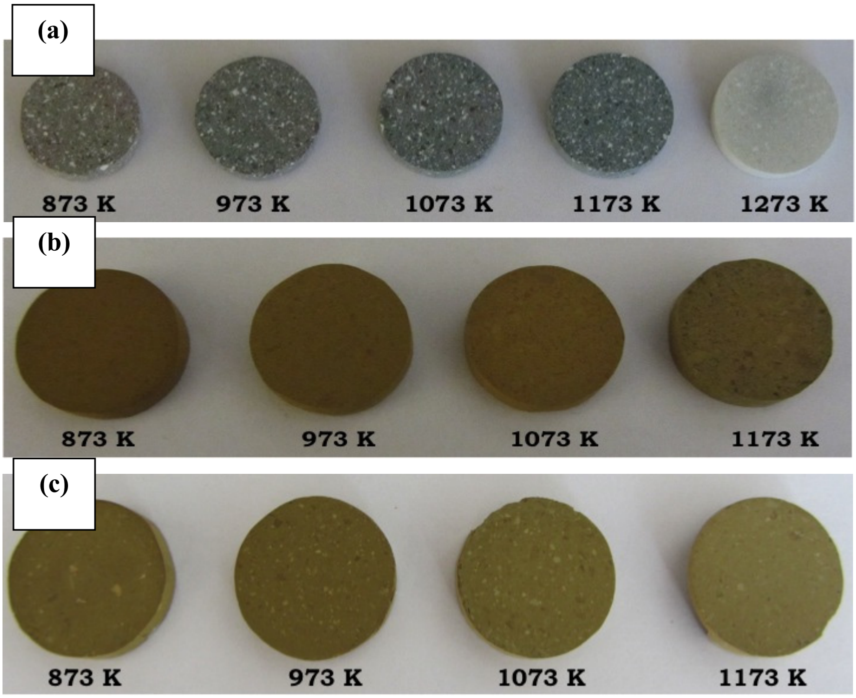

Fig. 3.12 PECS compacts of (a) magnetite-silica, (b) magnetite-silica-silver and (c) silica-silver hybrid coreshell powders

4. Discussion

4.1 Control of the stoichiometry, size and magnetic properties of magnetite nanoparticles

The synthesis of magnetite-core in Publication I was motivated by the results presented by Alibeigi and Vaezi (2008) and Mizukoshi et al. (2009). They demonstrated that magnetite nanoparticles can be produced by the reaction of only ferrous ion, Fe^{2+}, with an alkaline solution in ambient atmosphere. In this work, by applying a reverse co-precipitation method, the magnetite nanoparticles were produced under ambient atmosphere by varying the concentration of the iron precursor solutions from 0.05 to 1.0 M. Based on Alibeigi and Vaezi (2008), when the Fe^{2+} reacts with the precipitating agent OH^{-}, the following mechanisms may occur:

$$Fe^{2+} + 2OH^{-} \rightarrow Fe(OH)_2 \qquad (4.1)$$

$$Fe(OH)_2 \rightarrow FeOOH + Fe(OH)_3 \qquad (4.2)$$

$$2FeOOH + Fe(OH)_2 \rightarrow Fe_3O_4 + 2H_2O \qquad (4.3)$$

$$2Fe(OH)_3 + Fe(OH)_2 \rightarrow Fe_3O_4 + 4H_2O \qquad (4.4)$$

$$6Fe(OH)_2 + O_2 \rightarrow 2Fe_3O_4 + 6H_2O \qquad (4.5)$$

When Fe^{2+} is added into the base solution, iron (II) hydroxide [($Fe(OH)_2$] is formed (4.1). Part of $Fe(OH)_2$ will oxidize into iron oxide-hydroxide and iron (III) hydroxide, [FeOOH and $Fe(OH)_3$] (4.2). When iron oxide-hydroxide or iron (III) hydroxide reacts with $Fe(OH)_2$, magnetite forms as in (4.3) and (4.4). Another part of $Fe(OH)_2$ will be in direct contact with air, as the experiment is conducted in an ambient atmosphere, and form magnetite particles as shown in (4.5).

The XRD pattern showed magnetite reflection for the synthesized nanoparticles [Publication I]. However, as the reaction was conducted in air, the stoichiometry of the synthesized magnetite might change slightly. This is because the unstable Fe^{2+} cations in the inverse-spinel magnetite octahedral site can be oxidized into Fe^{3+} and cause changes in the magnetite stoichiometry, $x = Fe^{2+}/Fe^{3+} = 0.5$. This results in compounds ranging from partially oxidized magnetite, $Fe_{3-\delta}O_4$ ($0.5 < x < 0$; $0 < \delta < 0.33$), to fully oxidized magnetite, maghemite, γ-Fe_2O_3 ($x = 0$). As shown in Table 3.1 (pp. 36), the oxidation of magnetite depends on the synthesis protocol used. None of the synthesized particles showed maghemite stoichiometry, $Fe_{2.67}O_4$. Although only the ferrous ion was used as a magnetite precursor, the molar ratio of Fe^{2+}/Fe^{3+} did not exceed 0.5 (Alibeigi & Vaezi, 2008). Thus, even though the ferrous ion was slightly oxidized prior to the precipitating process, the final product should not be maghemite but partially oxidized/non-stoichiometric magnetite. In SP1, where Fe^{2+} was added drop-wise every ten minutes, stronger oxidation can be observed for low concentrations of ferrous ions. This increased oxidation is related to the very small particle size of the synthesized powder, 13 nm, resulting in a larger surface area for oxidation to occur. Nevertheless, morphology and particle size distribution are better controlled in SP1. Synthesis in which Fe^{2+} was added at once into the base solution (SP2) provided better oxidation control of the particles, with stoichiometry closer to that of magnetite. However, even though SP2 yielded better stoichiometry of magnetite, the morphology of the particles changed from spherical to an irregular morphology and the particle size increased as the Fe^{2+} concentration increased (Fig. 3.1, pp. 37). This morphology might also affect the saturation magnetization value. Based on Fig. 3.2 (pp. 38), the saturation magnetization value is apparently influenced by the stoichiometry of the magnetite nanoparticles, as the ferromagnetism of the magnetite nanoparticles is determined by the Fe^{2+} content in the octahedral sites of the inverse-spinel structure (Wang et al., 2004; Alibeigi & Vaezi, 2008). The M_S of bulk magnetite is 92 Am^2kg^{-1} and of nanopowder is 68 Am^2kg^{-1} (Wang et al., 2004). Oxidation of magnetite reduces the Fe^{2+} content, thus lowering the M_S value, as the M_S of bulk maghemite is 82 Am^2kg^{-1} and of nanopowder is 34–50 Am^2kg^{-1} (Alibeigi & Vaezi, 2008). Thus with stoichiometry closer to magnetite, higher M_S was expected. This correlation does not hold for SP2-0.6M particles that have their composition closest to magnetite. For these particles, the value of M_S is the lowest. Thus the irregular morphology and shape of the particles also seem to play a significant role in the magnetization behavior of magnetite nanoparticles, as proposed earlier by Song et al. (2012).

The results presented in Chapter 3.1 show that the most oxidized magnetite nanoparticles from SP2 have a stoichiometry of $Fe_{2.85}O_4$. When a low-temperature magnetic measurement is conducted on this powder, the results show that there is not a clear peak at the Verwey transition temperature, T_V (120 K), but only a broad peak in the regime. The absence of T_V might be caused by several factors, e.g., (i) particle size smaller than 50 nm or especially (ii) partial oxidation of magnetite to maghemite (Goya et al., 2003; Yang et al., 2004). The estimated Curie temperature, T_C, based on the decrease of the relative magnetization with temperature is 800 K. This is slightly lower than the standard T_C for magnetite, 850 K. It has been reported that T_C can be influenced by the cation vacancies in the iron oxide structures (Harrison & Putnis, 1996). As the particles stoichiometry, $Fe_{2.85}O_4$ is between pure magnetite (Fe_3O_4) and maghemite ($Fe_{2.67}O_4$), (i.e., partial oxidation of the magnetite occurs), cation vacancies will be formed due to the oxidation of Fe^{2+} in octahedral sites of the inverse-spinel structure into Fe^{3+}. The maximum occupancy of cation vacancies that leads to the formation of maghemite gives a T_C value of about 920 K (Restrepo, Labaye & Greneche, 2006). This behavior suggests that T_C is increased along with the number of cation vacancies. According to the estimation based on the XRD data, the synthesized magnetite nanoparticles not in exact magnetite stoichiometry, i.e., cation vacancies occured. However, the T_C of the particles does not increase but is slightly lower than that of the standard T_C of magnetite. Therefore the decrease of T_C with the increasing number of cation vacancies might be due to finite-size effects, i.e., T_C decreases as the particle size decreases (Wang et al., 2011).

Nevertheless, based on the unit cell calculation, almost all the reported magnetite nanoparticle synthesis procedures have resulted in non-stoichiometric magnetite (Vereda et al., 2008; Ozkaya et al., 2009) even though inert atmosphere has been used during the synthesis. This is due to the very large surface area of the nanoparticles, which are easily oxidized in air, even when exposed at room temperature (Murad & Schwertmann, 1993). This oxidized magnetite results in a deficiency of Fe^{2+} and decreases the magnetic properties, i.e., saturation magnetization of the particles. Thus an amorphous silica layer was introduced as a coating layer for the nanoparticles forming the coreshell structures. Other than preventing the oxide nanoparticles from further oxidation, the coreshell powder itself can be used for developing novel multifunctional materials, as discussed in Publications III–VII. A modified Stöber method was used in forming the silica shell. Based on the magnetic measurement, the saturation magnetization of the magnetite-silica coreshell structure dropped to 6.5 Am^2kg^{-1} as compared to that of bare magnetite nanoparticles, about 57 Am^2kg^{-1}. This is due to the small weight fraction of magnetite inside the silica. Nevertheless, the magnetite content in the silica structure can be estimated based on the amount used during the Stöber process by assuming that no magnetite was left out the silica shells after the process. It was found that the magnetization increased to 74 Am^2/kg at 300 K. This value is higher than that of bare particles, 57 Am^2kg^{-1}, and has quite a similar M_S value to that of less oxidized magnetite [Publication I]. The observation suggests that the silica shell can prevent further oxidation of the magnetite nanoparticles retaining higher magnetic saturation. In addition, the silica layer separates the agglomeration of particles and reduces the interparticle interactions, thus increasing the magnetization. The estimated Curie temperature for the magnetic measurements at 10 K, 300 K and 800 K is roughly 850 K, which is similar to that of standard magnetite. In addition, the Mössbauer results also suggested that magnetite is the phase present within the coreshell structure [Publication II]. In the case of the Verwey transition temperature, a similar observation was made with the bare magnetite nanoparticles, where there is only a broad peak around the temperature where the transition is expected. This broadness of transition can also be ascribed to the small size of the particles and their distribution.

In summary, by controlling the synthesis protocols of magnetite nanoparticles by using only ferrous ions in ambient atmosphere it is also possible to obtain high saturation magnetization value particles with stoichiometry closely approaching that of magnetite. The oxidation of the magnetite can be controlled by forming the amorphous silica layer as a coreshell structure. Within this structure, the magnetite phase can be retained (or kept less oxidized), as suggested by low-temperature magnetic measurement and fits of the Mössbauer spectra. In addition, with the silica layer, functionalization with silver or silver chloride particles is possible without prior surface modification, as discussed in the next section (Section 4.2).

4.2 Functionalization of the coreshell powders with Ag and AgCl

Silver-supported silica materials are expected to be excellent candidates for applications such as nanoprobes for biomedical application or antibacterial material. In the case of silver chloride, its photocatalytic behavior can be further expanded under the visible light region by combination with Ag nanoparticles. In addition, these hybrid coreshell structures can prevent the aggregation of the doping particles themselves, and with the addition of magnetic core they can be easily retrieved by applying an external magnetic field. For optimum properties, it is important to control the deposition and attachment of the particles on the silica surface. Thus in Publications III and IV, the mechanism of the silver or silver chloride attachments on the silica surface was studied. Based on the results it is suggested that the attachment/deposition results from the electrostatic interaction between $Ag(NH_3)_2^+$ complexes and the OH^- groups and hydrogen bonding between the PVP and silica-shell surface. In addition, Ag^+ itself can also form electrostatic attraction with the hydroxyl group of silica (Yang et al., 2012). PVP was used as a reducing agent for Ag ions in all four different synthesis approaches studied [Publication III]. In the solution, Ag^+ interacts with the non-bonding electrons of the oxygen atom in the PVP carbonyl group, forming the $Ag_m^{m+} - PVP$ complex (m = number of Ag^+ anchored in the PVP chain). Ag^+ is reduced by the charge transfer interaction and aggregates into large Ag particles (Wu et al., 2010). For Approach 2, since Ag^+ is reduced prior to mixing with silica, the attachment of the Ag particles on the silica surface is due to hydrogen bonding between the PVP and silica. This can be explained by the bonding site of the silanol group combined with the PVP molecular chains via hydrogen bonding force between the –OH and oxygen atom, O, on the carbonyl group of PVP (C=O), as shown in Fig. 4.1.

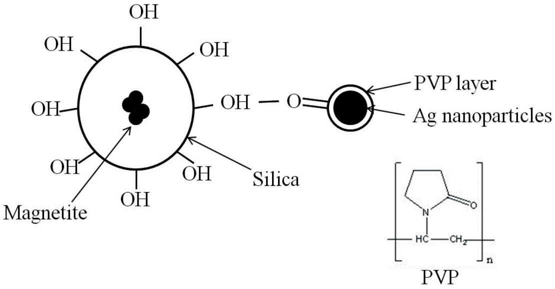

Fig. 4.1 Hydrogen bonding between the silanol and PVP carbonyl groups

As seen in Fig. 3.6 (pp. 43), reduction of Ag^+ can already be observed after 30 minutes of reaction. As no additional reducing agent was used, the weight ratio of PVP/$AgNO_3$ may play an important role, since in this process the reduction rate is strongly influenced by the weight fraction of PVP (He et al., 2002; Kim, 2007). In addition, PVP also acted as a capping agent by controlling the growth of the Ag particles (Ye et al., 2007), thus yielding non-agglomerated particles and quite uniform morphology with narrow size distributions of the particles. However, when the solution was contaminated with chloride ions, bigger particles with irregular morphology were observed. The formation of AgCl particles affected the size distribution in Approaches 3 and 4 (Table 3.2, pp. 44) and the deposition rate of Ag nanoparticles. This was due to the Ag^+ reacting with Cl^- instead of forming the Ag agglomerates. The deposition rate of Ag/AgCl was increased under ultrasonic mixing due to the microjets and shock waves that are created in the solution during the sonication process. This mechanism may enhance the affiliation of the ions, leading to the fast formation of the larger particles and pushing these particles toward the silica-shell, thus promoting their adherence to the surface (Suslick & Price, 1999).

Surface plasmon excitation of Ag particles appears at ~400 nm (Kim, 2007). Thus with silver doping, the solution containing hybrid coreshell powders showed a strong absorption peak at around 400 nm of wavelength. On the other hand, AgCl nanoparticles have a direct and indirect semiconductor band gap of 5.15 eV (~240 nm) and 3.25 eV (~380 nm), respectively (Currao et al., 2004). Therefore AgCl does not absorb in the visible wavelength region. With silver nanoparticles, the absorption was extended to the visible region due to the surface plasmon resonance absorption of silver. AgCl itself is known as a good candidate for photocatalytic activity (Currao et al., 2004; Chen et al., 2012), and with additional silver nanoparticles this photocatalytic behavior can be extended to the visible region. Thus contamination of AgCl during the preparation of magnetite-silica-silver coreshell structures [Publication III] has created a new idea in synthesizing both Ag and AgCl by using a similar synthesis approach, with the addition of chloride ions to promote the formation of AgCl. This idea is developed further in Publication IV.

In Publication IV, HCl was used to induce the formation of AgCl with PVP as a capping agent. As shown in Figs 3.7 and 3.8 (pp. 46–47), the deposition of AgCl particles on the silica-shells was difficult to control due to the very active reaction between the Ag^+ and Cl^-. Therefore an improvement was later made by controlling the ratio between $AgNO_3$ and HCl. In this approach, the aim was to obtain the size and shape of the AgCl particles in a controlled manner, as both size and shape have an important effect on the photocatalytic behavior of the particles (Zhu, Chen & Liu, 2011). As shown in Fig. 4.2, a cubic, nanosized AgCl was obtained. In addition, a new method was developed to produce both Ag and AgCl in a single run, which can be observed from the XRD pattern in Fig. 4.3. Most of the earlier work (Wang et al., 2008; Kim et al., 2010; Jiang & Zhang, 2011; An et al., 2012) reported that the Ag/AgCl structure was synthesized by first forming the AgCl, with Ag formed later on AgCl surfaces by reduction with chemicals or exposure to light/heat irradiation. In the current approach, AgCl and Ag are synthesized at the same time by modifying the procedure described in Publications III and IV. Such an approach is new and has not been reported before to the author's knowledge. This work is still ongoing.

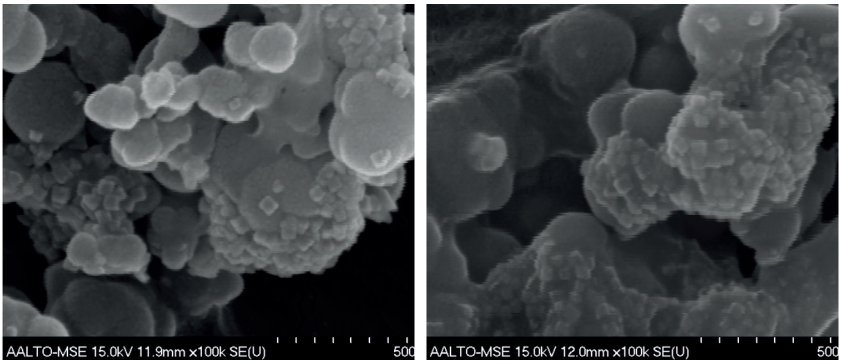

Fig.4.2 SEM image of Ag/AgCl-doped magnetite-silica coreshell structure

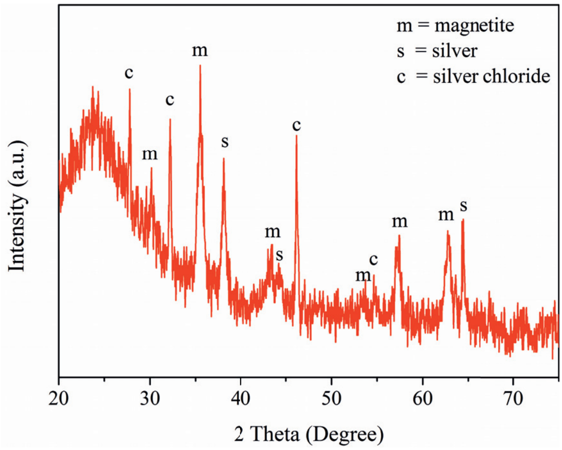

Fig. 4.3 XRD pattern of Ag/AgCl-doped magnetite-silica coreshell structure

The value of saturation magnetization of magnetite-silica coreshell powders is different after Ag or Ag/AgCl doping: 5.0, 8.4, 8.2 and 12.2 Am^2kg^{-1} for Approaches 1, 2, 3 and 4, respectively. The main reason for the differences is the magnetite content of the silica. Silica-shell, silver and silver chloride particles are diamagnetic and thus only negligibly contribute to the magnetization. It was shown that due to the agglomeration of the magnetite nanoparticles [Publication III, Fig. 1], the amount of ferromagnetic oxide powder varies in each of the silica spheres, which can cause variation in the magnetization. However, in a randomly selected powder, averaging of the number of particles in the magnetic measurement should reduce this effect. The saturation magnetization of magnetite powder is about 70–74 Am^2kg^{-1} [Publications I and II]. Using this value, the magnetite content inside the silica-shells for each approach is estimated to be about 7% (Approach 1), 12% (Approach 2), 12% (Approach 3) and 17% (Approach 4) of the sample mass. This must be taken only as a very rough estimation because the ferromagnetic iron oxide was prepared using two different molar concentrations, 0.05 M and 0.4 M, of Fe^{2+} [Publication III]. This results in different sizes of the magnetite nanoparticles, which influences the magnetization values [Publication I]. However, as the smaller nanoparticles have smaller moments, the volume of magnetite nanoparticles in the core can be comparable for both methods. However, the saturation magnetization values are still different, even though in both Approaches 1 and 2, powders contained magnetite synthesized from the same concentration (0.05 M of Fe^{2+}). A similar situation occurs in samples used in Approaches 3 and 4 with 0.4 M of Fe^{2+} concentration used. If we assume a similar amount of silica shell in all powders, the difference can be ascribed to different amounts of Ag particles attached on the shell. As the density of Ag is about twice the density of the magnetite powder, a larger amount of Ag would result in a significantly lower saturation magnetization value. The highest magnetization was associated with the Approach 4 sample having a low concentration of Ag as estimated from the UV-visible absorbance spectra [Publication III, Fig. 13]. On the other hand, the lowest magnetization was associated with the Approach 1 sample, which exhibits a very strong absorbance peak, suggesting that most of the SiO_2 particle surfaces were covered with Ag particles. Thus the difference in powder magnetization can most likely be explained by the difference in the amount of silver. In the case of Ag/AgCl-doped coreshell particles in Publication IV, the similar values (5 Am^2kg^{-1} on average) of M_S might be due to the rather similar deposition rates of each sample.

4.3 Properties of the compacts made of functionalized magnetite nanoparticles

Based on Publication V, it is clear that the magnetite content has a major influence on the transparency of the compacts made from magnetite-silica coreshell particles. A large amount of magnetite can cause structural changes in the glass network during the compaction, as indicated by the molar volume calculation [Publication V, Fig. 3] by forming non-bridging oxygen (NBO) (El-Hadi et al., 1991), i.e., Si-O-Fe^{2+} and Si-O-Fe^{3+}, which suggests that both Fe^{2+} and Fe^{3+} behave as network modifying ions (Salama & Salman, 1993; Mekki et al., 2000). These ions occupy the interstitial space of the amorphous SiO_2 network and reduce the crystallization energy, thus promoting crystallization at lower temperature (Salama & Salman, 1993; Wang, 2010). The crystallization temperature of Stöber silica determined from DSC analysis was 1451 K. With the magnetite-core, the crystallization of silica occurred at temperatures below 1451 K [Publications V–VII]. This supports the role of Fe^{3+} and Fe^{2+} as network modifying agents. It further suggests that both Fe^{3+} and Fe^{2+} might result from the reduction of the magnetite/iron oxide phase inside the compacts. Thus it can be assumed that a reducing environment is created during the compaction. Two possibilities for the creation of a reducing environment can be considered: first, the reducing environment might be created from the hydroxyl (OH) groups of silica; second, the reducing environment could be created in the PECS vacuum chamber via formation of carbon monoxide in the reaction of graphite with oxygen.

Let us consider the case of silica as a reducer. As explained in Chapter 1, Section 1.4, pp. 14, in amorphous silica the hydroxyl groups consist of silanol, geminals or vicinal/hydrogen-bonded silanols. In the silica matrix, under argon gas, the reducing atmosphere can be created from the vicinal silanols (Chaneac, Tronc & Jolivet, 1995). During heating, breaking up of vicinal silanols occurs in the temperature range 473–673 K (Vansant, Van Der Voort & Vrancken, 1995), in agreement with data developed by Zhuravlev (2000), where at 673 K, these vicinal silanols were destroyed. The cleavage of the hydrogen-bonded network creates a mild reducing atmosphere in the silica matrix and causes the reduction of the oxidized hematite into magnetite (Table 3.3). The DSC graph [Publication VI, Fig. 1c] shows broad exothermic peaks at 600 K. This might be because of the oxidation of magnetite into maghemite followed by hematite. The diffused endothermic peaks observed above 900 K may be due to the reduction of hematite to magnetite. Since the breaking up of the vicinal silanols occurred at 473–673 K, it can be assumed that at a temperature of 673 K and above, the reduction of iron oxide inside the silica matrix should occur. However in PECS at temperatures from 873 to 1173 K, no reduction of the iron oxide phase could be detected [Publication VII, Fig. 2b], where the XRD patterns show that magnetite remained unchanged or slightly oxidized, forming a small fraction of ε-Fe_2O_3 as suggested by the room-temperature magnetic measurement [Publication VII]. Meanwhile, in argon DSC, the reduction of iron oxide in sol-gel silica has already occurred at 773 K (Chaneac, Tronc & Jolivet, 1995). This condition explains why in the temperature range from 873 K to 1173 K in PECS no sign of the reduction process was noticed. This suggests that the reduction of magnetite by hydrogen from the breaking up of vicinal silanols of the silica shell in a vacuum did not take place. Thus it can be concluded that the silica matrix does not cause the reducing atmosphere during the PECS process.

The second consideration is based on a reducing environment that might be created during the PECS process. In PECS, the hybrid coreshell powders are sintered under a vacuum level of 9–15 Pa, in which the oxygen partial pressure, $p(O_2)$, is about 1.87–3.15 x 10^{-5} atm [Publications V–VII]. Depending on the sintering temperatures [Publications V–VII], the equilibrium partial pressure of oxygen for oxidation of carbon into carbon monoxide is in the range from 10^{-18} to 10^{-24} atm (Ellingham, 1994). The lower $p(O_2)$ equilibrium than $p(O_2)$ in a vacuum causes the graphite to oxidize and produce CO (i.e., a reducing environment) during the sintering process. In the Ellingham diagram (Ellingham, 1994), the line for $2C + O_2 \rightarrow 2CO$ falls below the oxidation lines for all the iron oxides when the temperature reaches 1073 K. Thus reduction of iron oxide above 1073 K should be possible [Publications V and VI]. In Publication VII the reduction environment may start to dominate only at 1173 K, as shown by the increment in magnetite peak intensity and crystallite size, and becomes more effective at higher temperatures. It seems that the efficiency of the created reducing atmosphere below 1273 K is insufficient (too mild) for reduction to occur during the short sintering cycle of PECS. The reducing environment created during the PECS process was further confirmed by compaction of commercial magnetite powder. Comparison can be made based on the XRD patterns of the powder before and after compaction in Fig. 4.4.

In Figure 4.4, the phase differences can be observed from the XRD patterns of the commercial magnetite powder before and after PECS compaction. Before compaction, there are clear peaks of magnetite with additional peaks from other iron oxides such as hematite and maghemite, which are impurities in the powder. After PECS, peaks iron oxide impurities disappear and part of the magnetite is reduced to wustite, FeO. This shows that a reducing atmosphere was created during the process. In addition, a strong peak of graphite, C, can be observed. This graphite comes from the graphite foil, which might not have been fully removed in the grinding process.

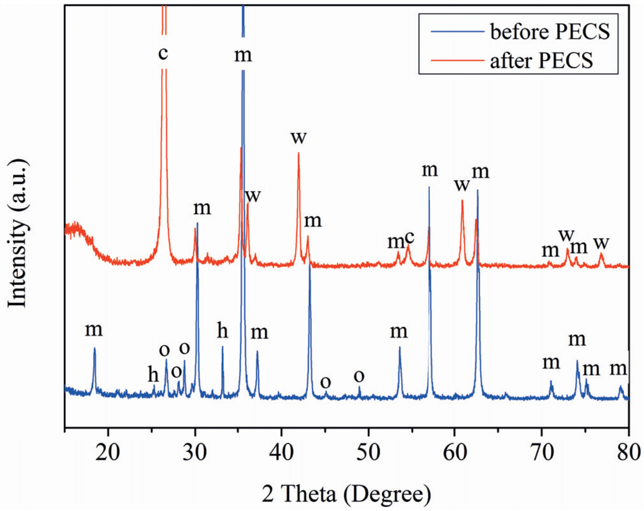

Fig. 4.4 XRD patterns of commercial magnetite powder before and after PECS compaction (m = magnetite, h = hematite, w = wustite, o = maghemite, c = graphite)

The reducing atmosphere created might also influence the redox behavior of iron ions by further reducing part of the Fe^{3+} into Fe^{2+} (El-Hadi et al., 1991). Guglielmi, Mashio and Molinari (1985) reported that Fe^{2+} has a major influence on the crystallization process of silica, but it does not affect the internal nucleation, which is induced by the Fe^{3+} ions, i.e., crystallization occurs only if both ferric and ferrous ions are present. With a sufficient amount of nucleating agent, the crystal growth should be catalyzed by a higher amount of Fe^{2+} ions (Salama and Salman, 1993; Mekki et al., 2000). This is in agreement with the XRD results in Publication V, as the crystallization is enhanced, with the higher amount of magnetite in the original powder perhaps promoting more Fe^{2+} ion formation. In Publication VI, higher magnetite contents were used, resulting in the domination of cristobalite phase over quartz. Nanri et al. (1996) reported that Fe^{3+} coexisting with Fe^{2+} accelerates the formation of cristobalite. Thus the higher the amount of magnetite added, the higher the amount of Fe^{3+} formed, which explains the domination of cristobalite peaks as the magnetite content increases (Figure 3.11, pp. 50). As a result of the phase transformation, crystallization of silica occurs. The crystallization of silica causes the molar volume to change and induces pores, which in addition to the grain growth causes the scattering of light passing through the material, resulting in loss of transparency. Other factors such as agglomeration of the starting powders may also contribute to the porosity of the sintered compacts.

However, different phenomena are observed for silver-containing magnetite-silica hybrid powders [Publication VII]. Magnetite was found to be oxidized into hematite, and the oxidation was more intensive at the maximum temperature used, 1173 K. Sintering was limited to 1173 K as the melting point of bulk silver is about 1233 K. From the XRD [Publication VII, Fig. 2c], silver oxides (Ag_2O and Ag_2O_3) were found in compacts sintered at 873 and 973 K. As the temperature increased up to 1073 and 1173 K, the peaks of silver oxides disappeared. These silver oxides are intermediate phases prior to the formation of Ag during annealing (Al-Kuhaili, 2007). Formation and decomposition of the silver oxides depend on both the oxygen partial pressure and the temperature (Tilley, 2008). In an environment with sufficiently high oxygen partial pressure, Ag_2O_3 can be formed at a temperature higher than ~673 K (Semaltianos et al., 2012). Thus the decomposition of Ag_2O_3 into Ag_2O and of Ag_2O into metallic Ag and O_2 was expected to occur at a temperature higher than 673 K. This explains why both of these silver oxides were still observed in the XRD pattern at temperatures as high as 873 and 973 K. The oxygen that is released from the thermal decomposition of silver oxides might diffuse into the silica and oxidize the Fe_3O_4 into α-Fe_2O_3, thus giving the mixture of peaks of Fe_3O_4 and α-Fe_2O_3 at 873 and 973 K, which is not observed for the compacts without silver. As the temperature increases up to 1073 and 1173 K, silver oxides peaks disappear and only the α-Fe_2O_3 can be observed.

The magnetic behaviors of the compacts are markedly different from those of the starting powders. For transparent compacts, diamagnetic behavior was observed for silica-free magnetite and a compact with 0.02 mol % of magnetite content [Publication V, Fig. 7]. Diamagnetism is a weak and repulsive effect of magnetism, which only exhibited by a diamagnetic substance in the presence of externally applied magnetic field (Cullity and Graham, 2009). Silica glass is a diamagnetic material (Cullity and Graham, 2009), thus showing a diamagnetic behavior in silica-free magnetite compact under an applied magnetic field. For compact with very small magnetite content (0.02%), the magnetic contribution was shielded by the diamagnetic behavior of the silica glass. This is caused by the distributed iron ions, which are paramagnetic, inside the diamagnetic glassy structure. Paramagnetic behavior was observed in compacts with 0.09 and 0.18 mol % of magnetite content with the slope of magnetization increased with increasing molar fraction of paramagnetic Fe ions. This paramagnetic behavior can be explained by the ‘shielding’ or frustration of the exchange interaction between metal ions due to the random nature of glass matrix (Mekki, 2001) and the large distance between iron ions. Ferromagnetic behavior of the compact (0.31 mol % magnetite) can be ascribed to the agglomeration of pure Fe clusters in the structure, as confirmed by XRD. The lower saturation magnetization of this compact compared to the starting powder might result from the paramagnetic contribution that was observed at a very low temperature magnetic measurement [Publication V, Fig. 8]. In

Publication VII, the increment of M_S may be due to the growth of the crystallite size of magnetite during the sintering (as indicated by the decrease of the FWHM values), as saturation magnetization of nanoparticles is lower due to magnetic surface reconstruction. When reduction of magnetite into pure Fe and crystallization of silica matrix occurred, the M_S value dropped due to the fine distribution of iron ions in the crystallized silica/glassy matrix, resulting in the paramagnetic state of Fe, in agreement with Publication V. A large drop in magnetization values occurred when magnetite was oxidized into hematite [Publication VII]. The drop was due to the very low magnetization of hematite itself, 0.4 Am^2kg^{-1} compared to 90 Am^2kg^{-1} for magnetite (Kletetschka, Wasilewski & Taylor, 2000).

5. Conclusions

On the basis of the results presented in this thesis and attached publications, the following conclusions can be drawn:

- Synthesis of magnetite nanoparticles in ambient atmosphere by a reverse co-precipitation from ferrous sulfate solution using NH_4OH as a precipitating agent at room temperature results in partially oxidized magnetite nanoparticles. Synthesis in which the iron salt precursor is added at once to the base solution (SP2) provides better oxidation control of the particles with closer stoichiometry to the magnetite than synthesis in which the precursor is added drop-wise (SP1). SP1 gives quite similar particle size and morphology at all concentrations of Fe^{2+}, while in SP2 the particles grow with irregular morphology as the concentration of Fe^{2+} increases. The saturation magnetization of SP1 powders increases when their composition approaches that of magnetite. The sudden decrease in saturation magnetization of SP2 powders at a composition closest to magnetite may be influenced by the irregular morphology of the powders.

- With silica coating, the saturation magnetization of the magnetite particles increases, probably because of better control of the oxidation of the magnetite particles. In addition, the Curie temperature of the magnetite-coreshell powder is similar to that of bulk pure magnetite, 850 K, showing that magnetite remains less oxidized in the silica-shell. This is also suggested by the Mössbauer results.

- For functionalizing of magnetite-coreshell structures with silver it was shown that a number of synthesis approaches are useful for the deposition of Ag nanoparticles on the silica-shell surfaces. A simple process was successfully introduced based on the reduction of the silver ions using PVP at room temperature. It was suggested that the deposition of Ag or Ag/AgCl on the silica shells occurs not only because of electrostatic attraction between Ag^+ or $Ag(NH_3)_2^+$ and the hydroxyl group of silica but also because of the hydrogen bonding and electrostatic attraction between the PVP and the silica surface. Reaction time does not have a strong influence on the further size evolution of Ag that has already formed after 30 min of synthesis, but it promotes the nucleation of Ag on the surface of silica. Irregular morphology can be observed in the chloride-contaminated samples, which affects their size distributions. All the powders prepared using the different synthesis approaches also show ferromagnetic behavior.

- For silver chloride functionalization of magnetite-coreshell structures, the size and shape of the AgCl particles depend on the concentration of HCl used. A very high concentration of Cl^- results in large particles with irregular cubic-like morphology, while very low Cl^- concentration results in the formation of small, irregular, nearly spherical AgCl nanoparticles. From optical measurement, a broad absorption in the UV-visible wavelength suggested the co-existence of Ag nanoclusters. Thus it is possible to produce nanosize AgCl particles by controlling the concentration of chloride ions. However, the deposition rate of AgCl nanoparticles is quite poor because of the rapid reaction between Ag^+ and Cl^-. An improvement was made in controlling the ratio of the silver precursor and the chloride ions.

- It is possible to produce transparent bulk magnetic compacts by the PECS method from magnetite-silica coreshell powders at low concentrations of magnetite (below 0.18 mol %). When the magnetite concentration of the magnetite-core nanoparticles used is higher, crystallization of the amorphous silica glass is induced at lower temperature. Crystallization is due to the reduction of the magnetite into pure iron by releasing the Fe^{2+} and Fe^{3+} ions that affect the silica network. It influences the transparency and the magnetization behavior of the compacts. It is suggested that the reduction of the magnetite during the compaction occurs because of the reducing atmosphere that was created from the reaction of graphite foils in a vacuum during the sintering process and that the effectiveness of the created atmosphere also depends on the PECS temperature.

- In Ag-containing magnetite-silica compacts, silver oxides were found to be intermediate phases during the formation of metallic Ag. Thermal decomposition of these oxides resulted in the oxidation of magnetite into hematite (α-Fe_2O_3). The formation of hematite caused a large drop in saturation magnetization values. The large coercivity value observed in the powder that was compacted at 1173 K suggests the presence of a small fraction of ε-Fe_2O_3.

Bibliography

Adams, A. P., Santschi, E. M. & Mellencamp, M. A. (1999) Antibacterial properties of a silver chloride-coated nylon wound dressing. *Veterinary Surgery*, 28 (4), 219–225.

Akimoto, S. (1954) Thermomagnetic study of ferromagnetic minerals contained in igneous rocks. *Journal of Geomagnetism and Geoelectricity*, 6, 1–14.

Alibeigi, S. & Vaezi, M. R. (2008) Phase transformation of iron oxide nanoparticles by varying the molar ratio of $Fe2^+$: $Fe3^+$. *Chemical Engineering & Technology*, 31 (11), 1591–1596.

Al-Kuhaili, M. F. (2007) Characterization of thin films produced by thermal evaporation of silver oxide. *Journal of Physics D: Applied Physics*, 40, 2847–2853.

An, C., Ming, X., Wang, J. & Wang, S. (2012) Construction of magnetic visible-light-driven plasmonic Fe_3O_4@SiO_2@AgCl:Ag nanophotocatalyst. *Journal of Materials Chemistry*, 22, 5171–5176.

Aono, H., Hirazawa, H., Naohara, T., Maehara, T., Kikkawa, H. & Watanabe, Y. (2005) Synthesis of fine magnetite powder using reverse coprecipitation method and its heating properties by applying AC magnetic field. *Materials Research Bulletin*, 40 (7), 1126–1135.

Ashtari, P., He, X., Wang, K. & Gong, P. (2005) An efficient method for recovery of target ssDNA based on amino-modified silica-coated magnetic nanoparticles. *Talanta*, 67 (3), 548–554.

Bahuguna, R., Mina, M., Tioh, J-W & Weber, R. J. (2006) Magneto-optic-based fiber switch for optical communications. *IEEE Transactions on Magnetics*, 42 (10), 3099–3101.

Berry, C. C., Wells, S., Charles, S. & Curtis, A. S. G. (2003) Dextran and albumin derivatised iron oxide nanoparticles: Influence on fibroblasts in vitro. *Biomaterials*, 24 (25), 4551–4557.

Beydoun, D., Amal, R., Low, G. & McEvoy, S. (2002) Occurrence and prevention of photodissolution at the phase junction of magnetite and titanium oxide. *Journal of Molecular Catalysis A: Chemical*, 180 (1–2), 193–200.

Beydoun, D., Amal, R., Low, G. K. C. & McEvoy, S. (2000) Novel photocatalyst: titania-coated magnetite. Activity and photodissolution. *Journal of Physical Chemistry B*, 104 (18), 4387–4396.

Bødker, F. & Mørup, S. (2000) Size dependence of the properties of hematite nanoparticles. *Europhysics Letters*, 52 (2), 217–223.

Boennemann, H., Brijoux, W., Brinkmann, R., Matoussevitch, N., Waldoefner, N., Palina, N. & Modrow, H. (2003) A size-selective synthesis of air stable colloidal magnetic cobalt nanoparticles. *Inorganica Chimica Acta*, 350, 617–624.

Bomati-Miguel, O., Leconte, Y., Morales, M. P., Herlin-Boime, N. & Veintemillas-Verdaguer, S. (2005) Laser pyrolysis preparation of SiO_2-coated magnetic nanoparticles for biomedical applications. *Journal of Magnetism and Magnetic Materials*, 290–291 (1), 272–275.

Bousnina, M. A., Omrani, A. D., Schoenstein, F., Madec, P., Haddadi, H., Smiri, L. S. & Jouini, N. (2010) Spark plasma sintering and hot isostatic pressing of nickel nanopowders elaborated by a modified polyol process and their microstructure, magnetic and mechanical characterization. *Journal of Alloys and Compounds*, 504 (Supplement 1), S323–S327.

Bragg, W. H. (1915) The structure of magnetite and the spinels. *Nature*, 95, 561.

Cannas, C., Ardu, A., Peddis, D., Sangregorio, C., Piccaluga, G. & Musinu, A. (2010) Surfactant-assisted route to fabricate $CoFe_2O_4$ individual nanoparticles and spherical assemblies. *Journal of Colloid and Interface Science*, 343 (2), 415–422.

Carotenuto, G., Pepe, G. P. & Nicolais, L. (2000) Preparation and characterization of nano-sized Ag/PVP composites for optical applications. *The European Physical Journal B*, 16, 11–17.

Caruana, L., Coasta, A. L., Cassani, M. C., Rampazzo, E., Prodi, L. & Zaccheroni, N. (2012) Tailored SiO_2-based coatings for dye doped superparamagnetic nanocomposites. *Colloids and Surfaces A: Physicochemical and Engineering Aspects*, 410, 111–118.

Chaneac, C., Tronc, E. & Jolivet, J. P. (1995) Thermal behavior of spinel iron oxide-silica composites. *Nanostructured Materials*, 6 (5), 715–718.

Chen, D., Yoo, S. H., Huang, Q., Ali, G. & Cho, S. O. (2012) Sonochemical synthesis of Ag/AgCl nanocubes and their efficient visible-light-driven photocatalytic performance. *Chemistry*, 18 (17), 5192–5200.

Chen, J., Wang, F., Huang, K., Liu, Y. & Liu, S. (2009) Preparation of Fe_3O_4 nanoparticles with adjustable morphology. *Journal of Alloys and Compounds*, 475 (1–2), 898–902.

Choi, M., Shin, K. H. & Jang, J. (2010) Plasmonic photocatalyst system using silver chloride/silver nanostructures under visible light. *Journal of Colloid and Interface Science*, 341 (1), 83–87.

Choi, R., Yang, J., Choi, J., Lim, E. K., Kim, E., Suh, J-S, Huh, Y-M & Haam, S. (2010) Thiolated dextran-coated gold nanorods for photothermal ablation of inflammatory macrophages. *Langmuir*, 26 (22), 17520–17527.

Choi, O., Deng, K. K., Kim, N. J., Ross, J. L., Surampalli, R. Y. & Hu, Z. (2008) The inhibitory effects of silver nanoparticles, silver ions, and silver chloride colloids on microbial growth. *Water Research*, 42 (12), 3066–3074.

Chou, K-S & Ren, C-Y (2000) Synthesis of nanosize silver nanoparticle by chemical reduction method. *Materials Chemistry and Physics*, 64, 241–246.

Clark, D. E. & Sutton, W. H. (1996) Microwave Processing of Materials, *Annual Review of Materials Science,* 26, 299–331.

Compeán-Jasso, M. E., Ruiz, F., Martínez, J. R. & Herrera-Gómez, A. (2008) Magnetic properties of magnetite nanoparticles synthesized by forced hydrolysis. *Materials Letters*, 62 (27), 4248–4250.

Cornell, R. M. & Schwertmann, U. (2003) *The iron oxides: Structures, properties, reactions, occurrences and uses*, 2nd edition. Weinheim, Wiley-VCH.

Cremer, G. D. (1944) Powder Metallurgy. U.S. Patent 2355954.

Cullity, B. D. & Graham, C. D. (2009) *Introduction to magnetic materials*, 2nd edition. New Jersey, John Wiley & Sons, Inc.

Cullity, B. D. & Stock, S. R. (2001) *Elements of X-ray diffraction*, 3rd edition. New Jersey, Prentice Hall.

Currao, A., Reddy, V. R., Veen, M. K. V., Schropp, R. E. I. & Calzaferri, G. (2004) Water splitting with silver chloride photoanodes and amorphous silicon solar cells. *Photochemical & Photobiological Sciences*, 3 (11–12), 1017–1025.

De Grave, E., Bowen, L. H., Amarasiriwardena, D. D. & Vandenberghe, R. E. (1988) ^{57}Fe Mössbauer effect study of highly substituted aluminum hematites: determination of the magnetic hyperfine field distributions. *Journal of Magnetism and Magnetic Materials*, 72 (2), 129–140.

Deng, Y-H, Wang, C-C, Hu, J-H, Yang, W-L & Fu, S-K (2005) Investigation of formation of silica-coated magnetite nanoparticles via sol-gel approach. *Colloids and Surfaces A*, 262, 87–93.

Dong, X., Lu, F., Yang, L., Zhang, Y. & Wang, X. (2008) Influence of spark plasma sintering temperature on electrochemical performance of $La_{0.80}Mg_{0.20}Ni_{3.75}$ alloy. *Materials Chemistry and Physics*, 112 (2), 596–602.

Dronskowski, R. (2001) The little maghemite story: A classic functional material. *Advanced Functional Materials*, 11 (1), 27–29.

Duval d'Adrian, A. L. (1922) Article of fused metallic oxide and process of producing the same. U.S. Patent 1430724.

El-Hadi, Z. A., Farouk, H., Khalifa, F. A. & Moustaffa, F. A. (1991) Molar volume of some sodium silicate and sodium borosilicate glasses. *Communications de la Faculté des Sciences de l'Université d'Ankara, Séries B*, 31, 49–57.

Ellingham, H. J. T. (1994) Reducibility of oxides and sulfides in metallurgical processes. *Journal of the Society of Chemical Industry*, 63, 125–133.

Evanoff, D. D. & Chumanov, G. (2005) Synthesis and optical properties of silver nanoparticles and arrays. *Chemphyschem*, 6 (7), 1221–1231.

Farrell, D., Majetich, S. A. & Wilcoxon, J. P. (2003) Preparation and characterization of monodisperse Fe nanoparticles. *The Journal of Physical Chemistry B*, 107 (40), 11022–11030.

Figuerola, A., Di Corato, R., Manna, L. & Pellegrino, T. (2010) From iron oxide nanoparticles towards advanced iron-based inorganic materials design for biomedical applications. *Pharmacological Research*, 62 (2), 126–143.

Flores, J. C., Torres, V., Popa, M., Crespo, D. & Calderon-Moreno, J. M. (2008) Variations in morphologies of silver nanoshells on silica spheres. *Colloids and Surfaces A: Physicochemical and Engineering Aspects*, 330 (1), 86–90.

Gaus, S. & Calzaferri, G. (2003) The band structures of the silver halides AgF, AgCl, and AgBr: A comparative study. *Photochemical & Photobiological Sciences*, 2, 398–401.

German, R. M. & Park, S. J. (2008) *Handbook of Mathematical Relations in Particulate Materials Processing: Ceramics, Powder Metals, Cermets, Carbides, Hard Materials, and Minerals*. Canada, John Wiley & Sons Inc.

Girginova, P. I., Daniel-da-Silva, A. L., Lopes, C. B., Figueira, P., Otero, M., Amaral, V. S., Pereira, E. & Trindade, T. (2010) Silica coated magnetite particles for magnetic removal of Hg^{2+} from water. *Journal of Colloid and Interface Science*, 345 (2), 234–240.

Gorski, C. A., Scherer, M. M. (2010) Determination of nanoparticulate magnetite stoichiometry by Mössbauer spectroscopy, acidic dissolution, and powder X-ray diffraction: A critical review. *American Mineralogist*, 95, 1017–1026.

Goya, G. F., Berquo, T. S., Fonseca, F. C. & Morales, M. P. (2003) Static and dynamic magnetic properties of spherical magnetite nanoparticles. *Journal of Applied Physics*, 94, 3520–3528.

Goya, G. F., Morales, M. P. (2004) Field dependence of blocking temperature in magnetite nanoparticles. *Journal of Metastable and Nanocrystalline Materials*, 20–21, 673–678.

Groza, J. R. (2007) Nanocrystalline powder consolidation methods. In: Koch C. C. (ed.) *Nanostructured Materials (2nd edition): Processing, Properties, and Applications*. William Andrew Inc., pp. 173–233.

Guardia, P., Batlle-Brugal, B., Roca, A. G., Iglesias, O., Morales, M. P., Serna, C. J., Labarta, A. & Batlle, X. (2007) Surfactant effects in monodisperse magnetite nanoparticles of controlled size. *Journal of Magnetism and Magnetic Materials*, 316, 756–759.

Guglielmi, M., Mashio, R. D. & Molinari, A. (1985) Crystallization of silica in SiO_2-Fe_2O_3 glasses obtained from gels. *Materials Chemistry and Physics*, 13, 171–177.

Guo, S., Li, D., Zhang, L., Li, J. & Wang, E. (2009) Monodisperse mesoporous superparamagnetic single-crystal magnetite nanoparticle for drug delivery. *Biomaterials*, 30 (10), 1881–1889.

Gupta, A. K. & Wells, S. (2004) Surface-modified superparamagnetic nanoparticles for drug delivery: Preparation, characterization and cytotoxicity studies. *IEEE Transactions on Nanobioscience*, 3 (1), 66–73.

Hägg, G. (1935) Die Kristallstruktur des manetischen Ferrioxyds, γ-Fe_2O_3. *Zeitschrift f¨ur Physikalische Chemie, Abteilung B: Chemie der Elementarprozesse, Aufbau der Materie* 29, 95–103.

Hakami, O., Zhang, Y. & Banks, C. J. (2012) Thiol-functionalised mesoporous silica-coated magnetite nanoparticles for high efficiency removal and recovery of Hg from water. *Water Research*, 46 (12), 3913–3922.

Harrison, R.J. & Putnis, A. (1996) Magnetic properties of the magnetite-spinel solid solution: Curie temperatures, magnetic susceptibilities, and cation ordering. *American Mineralogist*, 81, 375–384.

He, R., Qian, X., Yin, J. & Zhu, Z. (2002) Preparation of polychrome silver nanoparticles in different solvents. *Journal of Materials Chemistry*, 12, 3783–3786.

Hendriksen, P. V., Linderoth, S. & Lindgård, P. A. (1993) Finite-size modifications of the magnetic properties of clusters. *Physical Review B*, 48 (10), 7259–7273.

Hu, H., Wang, Z., Pan, L., Zhao, S. & Zhu, S. (2010) Ag-coated Fe_3O_4-SiO_2 three-ply composite microspheres: synthesis, characterization and application in detecting melamine with their surface-enhanced raman scattering. *The Journal of Physical Chemistry C*, 144 (17), 7738–7742.

Iglesias-Silva, E., Rivas, J., Isidro, L. M. L. & Lopez-Quintela, M. A. (2007) Synthesis of silver-coated magnetite nanoparticles. *Journal of Non-Crystalline Solids*, 353 (8–10), 829–831.

Inoue, K. (1967) Kiyoshi Inoue method of electrically sintering discrete bodies. U.S. Patent 3340052.

Inoue, K. (1966a) Electric Discharge Sintering. U.S. Patent 3241956.

Inoue, K. (1966b) Apparatus for electrically sintering discrete bodies. U.S. Patent 3250892.

Itoh, F. & Satou, M. (1975) Magnetic properties of iron oxide powder treated with sodium metaphosphate. *Japanese Journal of Applied Physics*, 14, 2091–2092.

Jiang, J. & Zhang, L. (2011) Rapid microwave-assisted nonaqueous synthesis and growth mechanism of AgCl/Ag, and its daylight-driven plasmonic photocatalysis. *Chemistry - A European Journal*, 17 (13), 3710–3717.

Jiang, Z-J, Liu, C-Y & Sun, L-W (2005) Catalytic properties of silver nanoparticles supported on silica spheres. *The Journal of Physical Chemistry B*, 109 (5), 1730–1735.

Jones, W. D. (1940) Powder metallurgy. *Metal Industry*, 56, 69–71.

Jun, B-H, Noh, M. S., Kim, J., Kim, G., Kang, H., Kim, M-S, Seo, Y-T, Baek, J., Kim, J-H, Park, J., Kim, S., Kim, Y-K, Hyeon, T., Cho, M-H, Jeong, D.H. & Lee, Y-S (2010) Multifunctional silver-embedded magnetic nanoparticles as SERS nanoprobes and their applications. *Small*, 6 (1), 119–125.

Kalele, S. A., Ashtaputre, S. S., Hebalkar, N. Y., Gosai, S. W., Deobangkar, D. N., Deobangkar, D. D. & Kulkarni, S. S. (2005) Optical detection of antibody using silica-silver core-shell particles. *Chemical Physics Letters*, 404 (1–3), 136–141.

Kalska-Szotsko, B., Rogowska, M., Dubis, A. & Szymanski, K. (2012) Enzymes immobilization on Fe_3O_4-gold nanoparticles. *Applied Surface Science*, 258 (7), 2783–2787.

Katz, J. D., Blake, R. D. & Scherer C. P. (1989) Microwave sintering of titanium diboride. *Ceramic Engineering and Science Proceedings*, 10, 857–867.

Kim, C. K., Lee, S., Shin, S. Y. & Kim, D. H. (2007) Microstructure and mechanical properties of Cu-base amorphous alloy matrix composites consolidate by spark plasma sintering. *Materials Science and Engineering A*, 449–451, 924–928.

Kim, J. S. (2007) Reduction of silver nitrate in ethanol by poly(N-vinyllpyrrolidone). *Journal of Industrial and Engineering Chemistry*, 13, 566–570.

Kim, S., Chung, H., Kwon, J. H., Yoon, H. G. & Kim, W. (2010) Facile synthesis of silver chloride nanocubes and their derivatives. *Bulletin of the Korean Chemical Society*, 31, 2918–2922.

Kletetschka, G., Wasilewski, P. J. & Taylor, P. T. (2000) Hematite vs. magnetite as the signature for planetary magnetic anomalies? *Physics of the Earth and Planetary Interiors*, 119 (3–4), 259–267.

Kobayashi, Y., Katakami, H., Mine, E., Nagao, D., Konn, M. & Liz-Marzan, L. M. (2005) Silica coating of silver nanoparticles using a modified Stöber method. *Journal of Colloid and Interface Science*, 283 (2), 392–396.

Krumme, J-P, Heitmann, H., Mateika, D. & Witter, K. (1977) MOPS, a magneto-opticphotoconductor sandwich for optical information storage. *Journal of Applied Physics*, 48 (1), 366–368.

Kumar, C. S. S. R. (2009) *Magnetic Nanomaterials: Nanomaterials for the Life Sciences*. Weinheim, Wiley-VCH.

Kura, H., Takahashi, M. & Ogawa, T. (2010) Synthesis of monodisperse iron nanoparticles with a high saturation magnetization using an Fe(CO)x-oleylamine reacted precursor. *The Journal of Physical Chemistry C*, 114 (13), 5835–5838.

Lange, F. F. (1989) Powder processing science and technology for increased reliability. *Journal of the American Ceramic Society*, 72 (1), 3–15.

Lee, J-M, Kim, D-W, Kim, T-H & Oh, S-G (2007) Facile route for preparation of silica-silver heterogeneous nanocomposite particles using alcohol reduction method. *Materials Letters*, 61 (7), 1558–1562.

Liu, X., Ma, Z., Xing, J. & Liu, H. (2004) Preparation and characterization of amino-silane modified superparamagnetic silica nanospheres. *Journal of Magnetism and Magnetic Materials*, 270 (1–2), 1–6.

Liu, Z. L., Wang, H. B., Lu, Q. H., Du, G. H., Peng, L., Du, Y. Q., Zhang, S.M. & Yao, K. L. (2004) Synthesis and characterization of ultrafine well-dispersed magnetic nanoparticles. *Journal of Magnetism and Magnetic Materials*, 283 (2–3), 258–262.

Lu, A-H, Salabas, E. L. & Schuth, F. (2007) Magnetic nanoparticles: synthesis, protection, functionalization, and application. *Angewandte Chemie (International ed. in English)*, 46 (8), 1222–1244.

Luo, N., Mao, L., Jiang, L., Zhang, J., Wu, Z., Wu, D. (2009) Directly ultraviolet photochemical deposition of silver nanoparticles on silica spheres: preparation and characterization. *Materials Letters*, 63 (1), 154–156.

Lu, Z., Dai, J., Song, X., Wang, G. & Yang, W. (2008) Facile synthesis of Fe_3O_4/SiO_2 composite nanoparticles from primary silica particles. *Colloids and Surfaces A: Physicochemical and Engineering Aspects*, 317 (1–3), 450–456.

Lv, B., Xu, Y., Tian, H., Wu, D. & Sun, Y. (2010) Synthesis of $Fe_3O_4/SiO_2/Ag$ nanoparticles and its application in surface-enhanced Raman scattering. *Journal of Solid State Chemistry*, 183 (12), 2968–2973.

Maher, B. A. (1988) Magnetic properties of some synthetic sub-micron magnetites. *Geophysical Journal International*, 94 (1), 83–96.

Maity, D., Choo, S-G, Yi, J., Ding, J. & Xue, J. M. (2009) Synthesis of magnetite nanoparticles via a solvent-free thermal decomposition route. *Journal of Magnetism and Magnetic Materials*, 321 (9), 1256–1259.

Margulies, D. T., Parker, F. T., Spada, F. E., Goldman, R. S., Li, J., Sinclair, R. & Berkowitz, A. E. (1996) Anomalous moment and anisotropy behavior in Fe_3O_4 films. *Physical Review B*, 53 (14), 9175–9187.

Marinescu, G., Patron, L., Culita, D. C., Neagoe, C., Lepadatu, C. I., Balint, I., Bessais, L. & Cizmas, C. B. (2006) Synthesis of magnetite nanoparticles in the presence of amino acids. *Journal of Nanoparticle Research*, 8 (6), 1045–1051.

Marques, R. F. C., Garcia, C., Lecante, P., Ribeiro, S. J. L., Noé, L., Silva, N. J. O., Amaral, V. S., Millán, A. & Verelst, M. (2008) Electroprecipitation of Fe_3O_4 nanoparticles in ethanol. *Journal of Magnetism and Magnetic Materials*, 320 (19), 2311–2315.

Mayerhöfer, T. G., Shen, Z., Leonova, E., Edén, M., Kriltz, A. & Popp, J. (2008) Consolidated silica glass from nanoparticles. *Journal of Solid State Chemistry*, 181 (9), 2442–2447.

McCormick, M. L., Bouwer, E. J. & Adriaens, P. (2002) Carbon tetrachloride transformation in a model iron-reducing culture: Relative kinetics of biotic and abiotic reactions. *Environmental Science & Technology*, 36 (3), 403–410.

Meisen, U. & Kathrein, H. (2000) Influence of particle size, shape and particle size distribution on properties of magnetites for the production of toners. *Journal of Imaging Science and Technology*, 44 (6), 508–513.

Mekki, A. (2001) Magnetic properties of Fe ions in a silicate glass and ceramic. *Physica Status Solidi (a)*, 184 (2), 327–333.

Mekki, A., Holland, D., Ziq, K. A. & McConville, C. F. (2000) Structural and magnetic properties of sodium iron germanate glasses. *Journal of Non-Crystalline Solids*, 272 (2–3), 179–190.

Melancon, M. P. & Li, C. (2009) Core–shell magnetic nanomaterials for medical diagnosis and therapy. In: Kumar, C. (ed.) *Magnetic Nanomaterials*. Weinheim, Wiley-VCH, pp. 259–290.

Millot, N., Le Gallet, S., Aymes, D., Bernard, F. & Grin, Y. (2007) Spark plasma sintering of cobalt ferrite nanopowders prepared by coprecipitation and hydrothermal synthesis. *Journal of the European Ceramic Society*, 27 (2–3), 921–926.

Mizukoshi, Y., Shuto, T., Masahashi, N. & Tanabe, S. (2009) Preparation of superparamagnetic magnetite nanoparticles by reverse precipitation method: contribution of sonichemically generated oxidants. *Ultrasonics Sonochemistry*, 16, 525–531.

Morales, M. P., Serna, C. J., Bødker, F. & Mørup, S. (1997) Spin-canting due to vacancy disorder in maghemite. *Journal of Physics: Condensed Matter*, 9, 5461–5467.

Morin, F. J. (1950) Magnetic susceptibility of αFe_2O_3 and αFe_2O_3 with added titanium. *Physical Review*, 78 (6), 819–820.

Murad, E. & Schwertmann, U. (1993) Temporal stability of a fine-grained magnetite. *Clays and Clay Minerals*, 41 (1), 111–113.

Murbe, J., Rechtenbach, A. & Töpfer, J. (2008) Synthesis and physical characterization of magnetite nanoparticles for biomedical applications. *Materials Chemistry and Physics*, 110 (2–3), 426–433.

Nanri, H., Takeuchi, N., Ishida, S., Watanabe, K. & Wakamatsu, M. (1996) Mineralizing action of iron in amorphous silica. *Journal of Non-Crystalline Solids*, 203, 375–379.

Nicula, R., Cojocaru, V. D., Stir, M., Hennicke, J. & Burkel, E. (2007) High-energy ball-milling synthesis and densification of Fe-Co alloy nanopowders by field-activated sintering (FAST). *Journal of Alloys and Compounds*, 434–435, 362–366.

Omori, M., Okubo, A., Gilhwan, K. & Hirai, T. (1997) Consolidation of thermosetting polyimide by the spark plasma system. *Journal of Materials Synthesis and Processing*, 4, 279–282.

Ozkaya, T., Toprak, M. S., Baykal, A., Kavas, H., Köseoglu, Y. & Aktas, B. (2009) Synthesis of Fe_3O_4 nanoparticle at 100°C and its magnetic characterization. *Journal of Alloys and Compounds*, 472, 18–23.

Pal, A., Shah, S. & Devi, S. (2009) Microwave-assisted synthesis of silver nanoparticles using ethanol as a reducing agent. *Materials Chemistry and Physics*, 114 (2–3), 530–532.

Pankhurst, Q. A., Connolly, J., Jones, S. K. & Dobson, J. (2003) Applications of magnetic nanoparticles in biomedicine. *Journal of Physics D: Applied Physics*, 36, R167–R181.

Quang, D. V., Sarawade, P. B., Hilonga, A., Park, S. D., Kim, J-K & Kim, H. T. (2011) Facile route for preparation of silver nanoparticle-coated precipitated silica. *Applied Surface Science*, 257 (9), 4250–4256.

Raguya, A. V. (2010). Fundamentals of spark plasma sintering. In: *Encyclopedia of Materials: Science and Technology*, pp. 1–5.

Raheman, F., Deshmukh, S., Ingle, A., Gade, A. & Rai, M. (2011) Silver nanoparticles: novel antimicrobial agent synthesized from an endophytic fungus *Pestalotia* sp. isolated from leaves of *Syzygium cumini* (L). *Nano Biomedicine and Engineering*, 3 (3), 174–178.

Raj, K. & Moskowitz, R. (1990) Commercial applications of ferrofluids. *Journal of Magnetism and Magnetic Materials*, 85 (1–3), 233–245.

Raming, T. P., Winnubst, A. J. A., van Kats, C. M. & Philipse, A. P. (2002) The synthesis and magnetic properties of nanosized hematite (α-Fe_2O_3) particles. *Journal of Colloid and Interface Science*, 249 (2), 346–350.

Ran, S., Vleugels, J., Huang, S., Vanmeensel, K., Blank, D. H. A. & Winnubst, L. (2010) Manipulating microstructure and mechanical properties of CuO doped 3Y-TZP nano-ceramics using spark plasma sintering. *Journal of the European Ceramic Society*, 30 (4), 899–904.

Restrepo, J., Labaye, Y. & Greneche, J. M. (2006) Surface anisotropy in maghemite nanoparticles. *Physica B: Condensed Matter*, 384 (1–2), 221–223.

Ross, W. F. (1945) Method and apparatus for making solid objects from metal powders. U.S. Patent 2372605.

Salama, S. N. & Salman, S. M. (1993) Crystallization characteristics of iron-containing spodumene-dopside glasses. *Journal of the European Ceramic Society*, 12, 61–69.

Santra, S., Tapec, R., Theodoropoulou, N., Dobson, J., Hebard, A. & Tan, W. (2001) Synthesis and characterization of silica-coated iron oxide nanoparticles in microemulsions: the effects of nonionic surfactants. *Langmuir*, 17 (10), 2900–2916.

Saravanan, P., Rao, K. S., Sivaprahasam, D. & Chandrasekaran, V. (2010) Consolidation of FePd nanoparticles by spark plasma sintering. *Intermetallics*, 18 (11), 2262–2265.

Schwertmann, U. (2008). Iron Oxides. In: Chesworth, W. (ed.) *Encyclopedia of Soil Science*, The Netherlands, Springer, pp. 363-369.

Schwertmann, U., Fitzpatrick, R. W., Taylor, R. M. & Lewis, D. G. (1979) The influence of aluminum on iron oxides. Part II. Preparation and properties of Al-substituted hematites. *Clays and Clay Minerals*, 27 (2), 105–112.

Semaltianos, N. G., Perrie, W., Romani, S., Potter, R. J., Dearden, G. & Watkins, K. G. (2012) Polymer-nanocomposites composed of PEDOT:PSS and nanoparticles of Ag synthesised by laser ablation. *Colloid and Polymer Science*, 290 (3), 213–220.

Sena, S. P., Lindley, R. A., Blythe, H. J., Sauer, C., Al-Kafarji, M. & Gehring, G. A. (1997) Investigation of magnetite thin films produced by pulsed laser deposition. *Journal of Magnetism and Magnetic Materials*, 176 (2–3), 111–126.

Song, M., Zhang, Y., Hu, S., Song, L., Dong, J., Chen, Z. & Gu, N. (2012) Influence of morphology and surface exchange reaction on magnetic properties of monodisperse magnetite nanoparticles. *Colloids and Surfaces A: Physicochemical Aspects*, 408, 114–121.

Spada, F. E., Berkowitz, A. E. & Prokey, N. T. (1991) H_C enhancement in partially reduced γ-Fe_2O_3 via surface treatment with sodium polyphosphate (revisited). *Journal of Applied Physics*, 69 (8), 4475–4477.

Stöber, W., Fink, A. & Bohn, E. (1968) Controlled growth of monodisperse silica spheres in the micron size range. *Journal of Colloid and Interface Science*, 26 (1), 62–69.

Suslick, K.S. & Price, G. J. (1999) Applications of ultrasound to materials chemistry. *Annual Review of Materials Science*, 29, 295–326.

Tang, B., Yuan, L., Shi, T., Yu, L. & Zhu, Y. (2009) Preparation of nano-sized magnetic particles from spent pickling liquors by ultrasonic-assisted chemical-co-precipitation. *Journal of Hazardous Materials*, 163 (2–3), 1173–1178.

Taylor, G. F. (February 1933) Apparatus for making hard metal composites. U.S. Patent 1896854.

Teja, A. S. & Koh, P-Y (2009) Synthesis, properties, and applications of magnetic iron oxide nanoparticles. *Progress in Crystal Growth and Characterization of Materials*, 55 (1–2), 22–45.

Teraoka, Y., Taura, Y., Moriguchi, I. & Kagawa, S. (1995) Preparation and catalytic activity for me thane oxidation of perovskite-type La(0.8)Sr(0.2)Mo(3) (M=CO, MN) with high-surface-area. *Kagaku Kogaku Ronbunshu*, 29, 1202–1203.

Thomas, S., Sakthikumar, D., Joy, P. A., Yoshida, Y., Anantharaman, M. R. (2006) Optically transparent magnetic nanocomposite based on encapsulated Fe_3O_4 nanoparticles in a sol–gel silica network. *Nanotechnology*, 17 (22), 5565–5573.

Tilley, R. J. D. (2008) *Defects in solids*. New Jersey, John Wiley & Sons.

Tronc, E., Ezzir, A., Cherkaoui, R., Chaneac, C., Nogues, M., Kachkachi, H., Fiorani, D., Testa, A. M., Greneche, J. M. & Jolivet, J. P. (2000) Surface-related properties of γ-Fe_2O_3 nanoparticles. *Journal of Magnetism and Magnetic Materials*, 221 (1–2), 63–79.

Vansant, E. F., Van Der Voort, P., Vrancken, K. C. (1995) Characterization and Chemical Modification of Silica Surface. Amsterdam, Elsevier.

Varanda, L. C., Jafelicci, M., Goya, G. F. (2001) Magnetic properties of spindle-type iron fine particles obtained from hematite. *Journal of Magnetism and Magnetic Materials*, 226–230, 1933–1935.

Vereda, F., de Vicente, J., Morales, M. P., Rull, F. & Hidalgo-Alvarez, R. (2008) Synthesis and characterization of single-domain monocrystalline magnetite particles by oxidative ageing of $Fe(OH)_2$. *The Journal of Physical Chemistry C*, 112 (15), 5843–5849.

Verwey, E. J. W. (1939) Electronic conduction in magnetite (Fe_3O_4) and its transition point at low temperatures. *Nature*, 144 (3642), 327–328.

Voogt, F. C., Palstra, T. T. M., Niesen, L., Rogojanu, O. C., James, M. A. & Hibma, T. (1998) Superparamagnetic behavior of structural domains in epitaxial ultrathin magnetite films. *Physical Review B*, 57 (14), R8107–R8110.

Wan, J., Li, H. & Chen, K. (2009) Synthesis and characterization of Fe_3O_4@ZnO core-shell structure nanoparticles. *Materials Chemistry and Physics*, 114 (1), 30–32.

Wang, C., Zhao, Z. (2009) Transparent $MgAl_2O_4$ ceramic produced by spark plasma sintering. *Scripta Materialia*, 61 (2), 193–196.

Wang, J., Chen, Q., Li, X., Shi, L., Peng, Z. & Zeng, C. (2004) Disappearing of the Verwey transition in magnetite nanoparticles synthesized under a magnetic field: implications for the origin of charge ordering. *Chemical Physics Letters*, 390 (1–3), 55–58.

Wang, J., Wu, W., Zhao, F. & Zhao, G-M (2011) Curie temperature reduction in SiO_2-coated ultrafine Fe_3O_4 nanoparticles: quantitative agreement with a finite-size scaling law. *Applied Physics Letters*, 98 (8), 083107.

Wang, P., Huang, B., Qin, X., Zhang, X., Dai, Y., Wei, J. and Whangbo, M-H (2008) Ag@AgCl: A highly efficient and stable photocatalyst active under visible light. *Angewandte Chemie International Edition*, 47 (41), 7931–7933.

Wang, S. (2010) Effects of Fe on crystallization and properties of a new high infrared radiance glass-ceramics. *Environmental Science and Technology*, 44 (12), 4816–4820.

Watson, S., Beydoun, D. & Amal, R. (2002) Synthesis of a novel magnetic photocatalyst by direct deposition of nanosized TiO_2 crystals onto a magnetic core. *Journal of Photochemistry and Photobiology A: Chemistry*, 148 (1–3), 303–313.

Weissleder, R. (2001) A clearer vision for in vivo imaging. *Nature Biotechnology*, 19, 316–317.

Wiley, B. J., Im, S. H., Li, Z-Y, McLellan, J., Siekkinen, A. & Xia, Y. (2006) Maneuvering the surface plasmon resonance of silver nanostructures through shape-controlled synthesis. *The Journal of Physical Chemistry B*, 110 (32), 15666–15675.

Wu, C., Mosher, B. P., Lyons, K. & Zeng, T. (2010) Reducing ability and mechanism for polyvinylpyrrolidone (PVP) in silver nanoparticles synthesis. *Journal of Nanoscience and Nanotechnology*, 10, 2342–2347.

Xu, J., Yang, H., Fu, W., Du, K., Sui, Y., Chen, J., Zeng, Y., Li, M. & Zou, G. (2007) Preparation and magnetic properties of magnetite nanoparticles by sol-gel method. *Journal of Magnetism and Magnetic Materials*, 309 (2), 307–311.

Xu, R., Wang, D., Zhang, J. & Li, Y. (2006) Shape-dependent catalytic activity of silver nanoparticles for the oxidation of styrene. *Chemistry, an Asian Journal*, 1 (6), 888–893.

Yamaguchi, K., Matsumoto, K. & Fuji, T. (1990) Magnetic anisotropy by ferromagnetic particles alignment in a magnetic field. *Journal of Applied Physics*, 67, 4493–4495.

Yan, S., Yin, J. & Zhou, E. (2006) Synthesis of NiZn ferrite-silica nanocomposites with a novel watermelon-like structure. *Colloids and Surfaces A: Physicochemical and Engineering Aspects*, 287 (1–3), 153–157.

Yang, H., Liu, Y., Shen, Q., Chen, L., You, W., Wang, X. & Sheng, J. (2012) Mesoporous silica microcapsules-supported Ag nanoparticles fabricated via nano-assembly and its antibacterial properties. *Journal of Materials Chemistry*, 22, 24132–24138.

Yang, J. B., Zhou, X. D., Yelon, W. B. & James, W. J. (2004) Magnetic and structural studies of the Verwey transition in $Fe_{3-\delta}O_4$ nanoparticles. *Journal of Applied Physics*, 95 (11), 7540–7542.

Yasumori, A., Matsumoto, H., Hayashi, S. & Okada, K. (2000) Magneto-optical properties of silica gel containing magnetite fine particles. *Journal of Sol-Gel Science and Technology*, 18 (3), 249–258.

Ye, X., Zhou, Y., Chen, J. & Sun, Y. (2007) Deposition of silver nanoparticles on silica spheres via ultrasound irradiation. *Applied Surface Science*, 253 (14), 6264–6267.

Yoon, S., Dornseiffer, J., Xiong, Y., Gruner, D., Shen, Z., Iwaya, S., Pithan, C. & Waser, R. (2011) Synthesis, spark plasma sintering and electrical conduction mechanism in $BaTiO_3$–Cu composite. *Journal of the European Ceramic Society*, 31, 773–782.

Yu, J. H., Wang, C. B., Shen, Q. & Zhang, L. M. (2012) Preparation and properties of Si_p/Al composites by spark plasma sintering. *Materials & Design*, 41, 198–202.

Zamani, M., Ghanaatshoar, M. & Alisafaee, H. (2011) Adjustable magneto-optical isolators with high transmittance and large Faraday rotation. *Journal of the Optical Society of America B*, 28, 2637–2642.

Zhang, D. B., Cheng, H. M. & Ma, J. M. (2001) Synthesis of silver-coated silica nanoparticles in nonionic reverse micelles. *Journal of Materials Science Letters*, 20 (5), 439–440.

Zhang, M., Cushing, B. L. & O'Connor, C. J. (2008) Synthesis and characterization of monodisperse ultra-thin silica-coated magnetic nanoparticles. *Nanotechnology*, 19 (8), 085601.

Zhang, X., Niu, H., Yan, J. & Cai, Y. (2011) Immobilizing silver nanoparticles onto the surface of magnetic silica composite to prepare magnetic disinfectant with enhanced stability and antibacterial activity. *Colloids and Surfaces A: Physicochemical and Engineering Aspects*, 375 (1–3), 186–192.

Zhu, M., Chen, P. & Liu, M. (2011) Sunlight-driven plasmonic photocatalysts based on Ag/AgCl nanostructures synthesized via an oil-in-water medium: enhanced catalytic performance by morphology selection. *Journal of Materials Chemistry*, 21, 16413–16419.

Zhuravlev, L. T. (2000) The surface chemistry of amorphous silica. Zhuravlev model. *Colloids and Surfaces A: Physicochemical and Engineering Aspects*, 173, 1–38.

Errata

Publication I

On page 3, line 2, the $Fe_{2.76}O_4$ should be written as $Fe_{2.67}O_4$.

Aalto-DD 58/2013

ISBN 978-952-60-5105-5
ISBN 978-952-60-5106-2 (pdf)
ISSN-L 1799-4934
ISSN 1799-4934
ISSN 1799-4942 (pdf)

Aalto University
School of Chemical Technology
Department of Materials Science and Engineering
www.aalto.fi